Contents lists available at ScienceDirect

Geochimica et Cosmochimica Acta

journal homepage: www.elsevier.com/locate/gca

Evidence for protracted fluid mobility from $^{40}Ar/^{39}Ar$ stepwise crushing of quartz-rich veins and high-grade rocks

Intan Chalid [a,*] , Jan R. Wijbrans [a] , Yang Wu [a,b] , Simona Ferrando [c,d] , Sander Hoogendoorn [e] , Leo M. Kriegsman [f,g] , Klaudia F. Kuiper [a]

[a] Department of Earth Sciences, Vrije Universiteit Amsterdam, De Boelelaan 1100, 1081 HV Amsterdam, the Netherlands
[b] Key Laboratory of Tectonics and Petroleum Resources (China University of Geosciences, Wuhan), Ministry of Education, Wuhan 430074, China
[c] Department of Earth Sciences, University of Torino, Via Valperga Caluso 35, 10125 Torino, Italy
[d] Consiglio Nazionale delle Ricerche – Istituto di Geoscienze e Georisorse (CNR-IGG), Sezione di Torino, Via Valperga Caluso 35, 10125 Torino, Italy
[e] Environment, Earth and Ecosystems Department, the Open University, Walten Hall, Milton Keynes, MK7 6AA, United Kingdom
[f] Research & Education Division, Naturalis Biodiversity Center, Darwinweg 2, 2333 CR Leiden, the Netherlands
[g] Department of Earth Sciences, Utrecht University, Princetonlaan 8A, 3584CB Utrecht, the Netherlands

ARTICLE INFO

ABSTRACT

Several decades of research into the tectonics, metamorphic petrology, and geochronology of the Agly Massif and adjacent areas, eastern Pyrenees (France) have revealed a complex tectono–metamorphic history including Variscan magmatism, Cretaceous tectono–metamorphic overprinting, and subsequent Alpine uplift and exhumation during the Cenozoic. However, the timescale and episodicity of fluid mobility in the area remain poorly constrained. In this study, we present stepwise crushing $^{40}Ar/^{39}Ar$ data from quartz-rich veins and high-grade rock samples, and fluid inclusion analyses that reveal the presence of brines (ca. 25–26 wt% NaCl equivalent ($NaCl_{eq}$)).

The stepwise crushing analysis was performed to liberate fluid from inclusions and evaluate its association with tectono–metamorphic processes. This approach allows to resolve distinct reservoirs of fluids, which can be identified chemically and isotopically using three-isotope correlation diagrams. The inverse isochron diagrams further facilitate the distinction between primary and secondary isotopic alignments. The results indicate the occurrence of several fluid pulses that produced new quartz veins at ~140 Ma, ~120–90 Ma, and ~80–60 Ma, while also affecting both earlier formed quartz-rich veins and high-grade rocks. These specific age groups relate to separate phases of fluid mobility induced by Cretaceous crustal extension and later exhumation during Paleogene convergence. Our findings put published maximum apparent ages into the context of episodic deformation and fluid activity and testify to the pervasive nature of fluid–rock interaction in the area.

1. Introduction

Fluids play a critical role in determining the thermal and chemical evolution of the continental crust and significantly affect the interpretation of radioisotopic ages. Fluid–rock interactions can partially or entirely reset isotopic systems, complicating the distinction between crystallization ages, thermal overprints, and cooling histories. The eastern Pyrenees exhibits such complexity, with a multiphase tectono–metamorphic and fluid evolution documented by several isotope systems. High-temperature geochronometers such as U–Th–Pb define the chronology of Variscan metamorphism and magmatism (Vanardois et al., 2022), whereas $^{40}Ar/^{39}Ar$ dating of muscovite and biotite yields

Cretaceous ages of ~120 to ~90 Ma, interpreted as progressive resetting and recrystallization during post-Variscan overprinting (Aumar et al., 2022). Cretaceous albitization has been dated to ~117 Ma by $^{40}Ar/^{39}Ar$ analysis of muscovite, and to 110 ± 8 Ma and 98 ± 2 Ma, through U–Th–Pb dating of monazite, reflecting pervasive fluid–rock interaction locally (Poujol et al., 2010). Thermochronological data applying apatite fission–track and apatite (U–Th)/He analyses reveal a late-stage, final uplift since the mid-Miocene (Yelland, 1990; Ternois et al., 2019).

In the Cretaceous, the reactivation of the Variscan basement units in response to extensional tectonics resulted in the formation of a system of shear zones, which acted as pathways for hydrothermal fluid flow. These fluids may have originated from devolatilization reactions of their wall

rocks, the infiltration of externally derived fluids, or a combination of both (Yardley, 1983; Bons, 2001; Philpotts and Ague, 2009). Repeated episodes of fracturing and fluid infiltration in the Axial Zone of the Pyrenees resulted in syn- and post-metamorphic fluid–rock interactions (Abd Elmola et al., 2018; Fig. 1).

Most geochronological studies in the Agly Massif have focused on minerals formed during metamorphic events and granitic intrusions (Vauchez et al., 2013; Guille et al., 2019; Odlum and Stockli, 2019; Ternois et al., 2019; Poitrenaud et al., 2020; Siron et al., 2020; Aumar et al., 2022). In contrast, the timing of fluid mobility as potentially recorded by ^{40}Ar/^{39}Ar dating of fluid inclusions in vein-hosted quartz remains poorly constrained. Although the quartz crystal lattice does not incorporate structural potassium, hydrous fluids trapped within fluid inclusions may contain significant amounts of potassium (Rauchenstein-Martinek, 2014; Bai et al., 2022; Xiao et al., 2022b). The ^{40}Ar/^{39}Ar stepwise crushing technique therefore represents a powerful means for dating fluids trapped in fluid inclusions of vein minerals and can be used to constrain the timing of fluid mobility (Di Vincenzo et al., 2004; Qiu et al., 2011; Shi et al., 2018; Hu et al., 2022; Monié et al., 2023).

Our study provides maximum apparent age information on the major phases of fluid mobility and their relationship to the tecto-no–metamorphic events in the formation of quartz veins and other high-grade rocks, based on ^{40}Ar/^{39}Ar analyses of quartz by stepwise crushing. These results provide new constraints on a protracted, regional-scale pulsed fluid circulation that influenced isotopic mobility, contributed to tectonic reactivation, and facilitated thermal overprinting of the Variscan basement rocks.

## 2. Geological background and sample selection

The rock basement of the Agly Massif originally formed during convergence along the margins of the Eurasian Plate during the Devonian and Carboniferous, and subsequently experienced crustal extension during the opening of the Gulf of Biscay in the Early to Late Cretaceous (Odlum and Stockli, 2019; Vanardois et al., 2022). Renewed convergence and concomitant uplift started in the Cretaceous to Late Cenozoic (Olivetti et al., 2020). Several key geologic events can be grouped into three principal periods that have impacted the region:

1. The Variscan orogenic belt was formed during a period of convergence approximately 370 to 290 Ma (Olivier et al., 2008; Poujol et al., 2010; Cochelin et al., 2017; Tournaire et al., 2018), and affected Late Proterozoic to Carboniferous sediments, as well as Ordovician granitoids, and, locally, Cadomian basement. The Variscan orogeny also led to high- temperature/low-pressure metamorphism up to anatexis and a significant volume of magmatic intrusions (Zwart, 1979). Granulite-facies rocks such as charnockite intrusives are only exposed in the northern Pyrenees, including the southern border of the Agly Massif (Vielzeuf and Kornprobst, 1984; Odlum and Stockli, 2019). Late-orogenic collapse (Permian) of the hot orogen is well documented (e.g., Van den Eeckhout and Zwart,
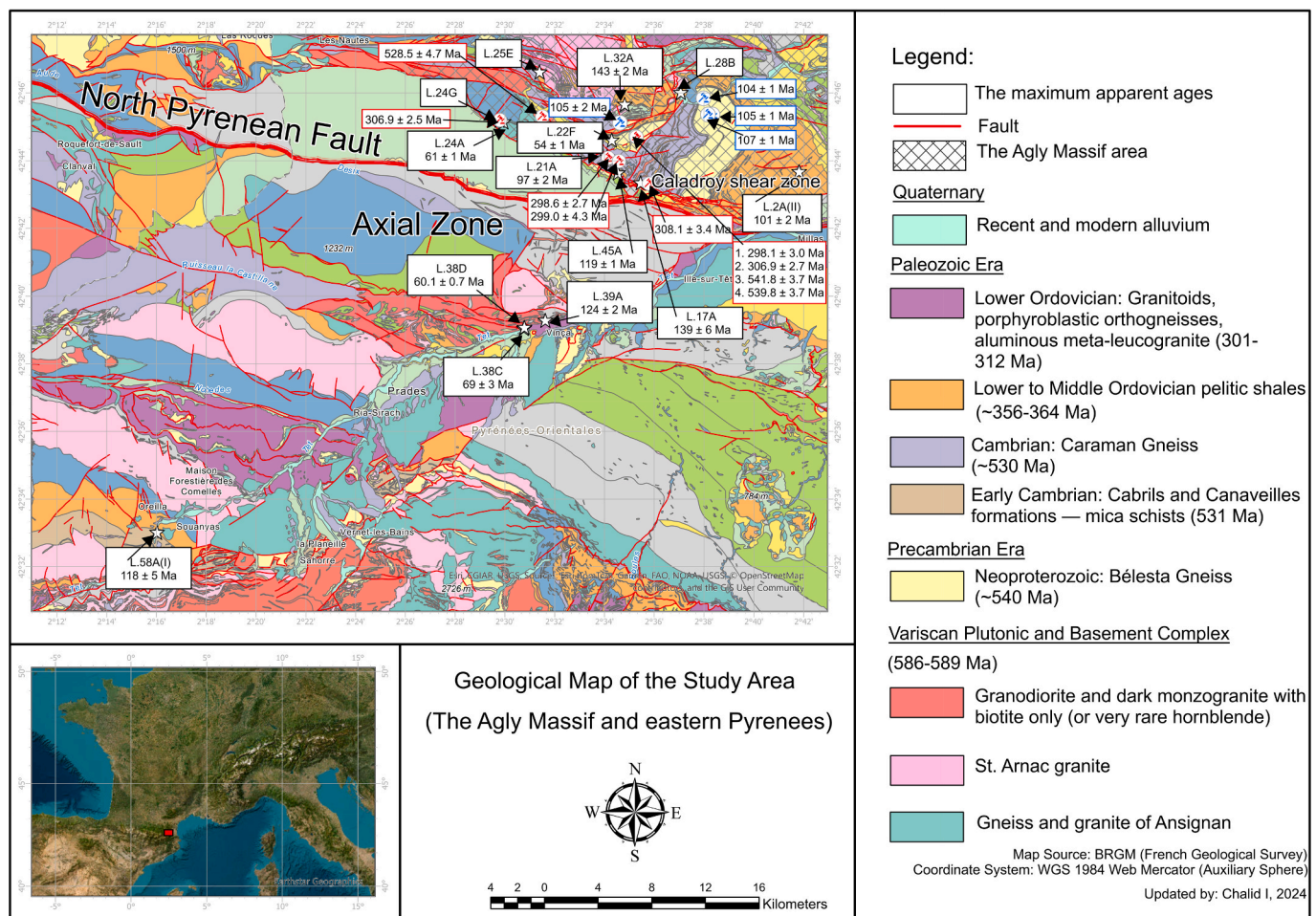
Fig. 1. Geological map of the Agly Massif and adjacent areas in the eastern Pyrenees, showing maximum apparent ages derived from stepwise crushing ^{40}Ar/^{39}Ar dating. Those without age labels correspond to inconclusive samples. Red outline boxes lacking sample numbers indicate zircon U–Pb ages of granite, orthogneiss, charnockite, and granodiorite as reported by Guille et al. (2019), whereas blue outlines represent ^{40}Ar/^{39}Ar ages from Aumar et al. (2022). Map source: https://www.brgm.fr.

1988; Vissers 1992), and together with erosion led to an unconformity overlain by Mesozoic sediments.

2. The Late Jurassic to the Paleocene (from *ca.* 150 to 60 Ma) was first marked by an extensional regime caused by rifting coevally with the opening of the Gulf of Biscay. In the Early to Late Cretaceous (~125 Ma to 83 Ma; Ogg et al., 2004), collision between the Iberian and European tectonic plates began, leading to severe thermal overprinting, significant uplift and reactivation of fault zones during the early stages of the Pyrenean orogenesis (Denèle et al., 2009, 2014; Mezger and Gerdes, 2014; Lagabrielle et al., 2016; Poujol et al., 2017).

3. The Paleogene to Neogene period (from *ca.* 56 to 23 Ma) was characterized by a series of extensional tectonic and depositional events that significantly influenced the formation of faults and the topographic growth reaching elevations of ~1000 to over 3000 m in the Pyrenees region (Burbank et al., 1992; Rosenbaum et al., 2002; Whitchurch et al., 2011; Ford et al., 2016; Honegger et al., 2021). Finally, the period from the early Miocene to the present has been studied by apatite fission–track and apatite helium dating
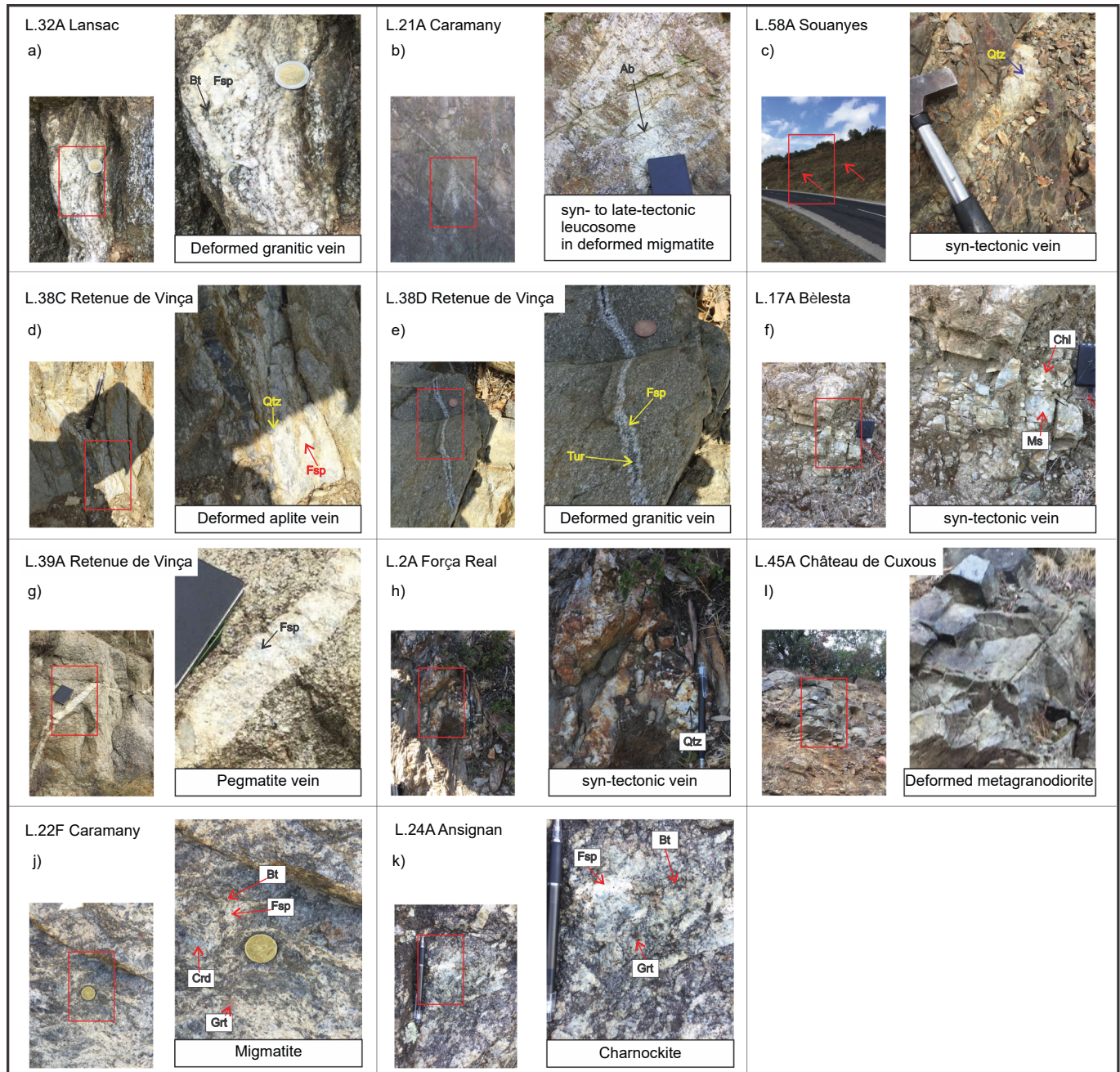
Fig. 2. Example of quartz-rich veins and high-grade rocks indicating fluid mobility in different geological formations. (**a**) L.32A – deformed granitic vein interpreted as a leucosome with a mylonitic groundmass. (**b**) L.21A – *syn-* to late-tectonic leucosome in deformed migmatite forms an altered white layer predominantly composed of quartz, feldspar, and micas, with some garnet. (**c**) L.58A – *syn-*tectonic vein filled with quartz and micas. (**d**) L.38C – deformed aplite vein within a ductile shear zone exhibiting a pale blueish colouration on its surface. (**e**) L.38D – deformed granitic vein exhibiting a distinct cross-cutting vein with a black, tourmaline-rich core, and quartz-feldspar assemblages along the margins. (**f**) L.17A – *syn-*tectonic vein with chlorite and mica group. (**g**) L.39A – pegmatite vein that consists of quartz, feldspar, and micas. (**h**) L.2A – *syn-*tectonic vein composed entirely of quartz. (**i**) L.45A – deformed metagranodiorite. (**j**) L.22F – migmatite consisting of feldspar, biotite, cordierite, and garnet. (**k**) L.24A – charnockite comprises quartz, biotite, feldspar, orthopyroxene, and garnet.

techniques, revealing geological processes related to tectonic activity, erosion, and topographic changes (*e.g.,* Maurel et al., 2008; Barbarand et al., 2018).

The sampling area is located in the Agly Massif and the adjacent domains situated in southern France, near the town of Prades (Fig. 1), and cover approximately 1,500 km². While the rocks reveal a range of metamorphic conditions between greenschist facies and granulite facies, the collected vein samples show evidence for new vein formation and overprinting of older veins under greenschist to lower amphibolite facies conditions. The veins are composed primarily of quartz and varying amounts of feldspar, mica, and chlorite-group minerals with accessory ilmenite, titanite, and apatite.

3. Methods

3.1. Materials and sample preparation

Our fieldwork revealed a variety of geological structures, including quartz boudins, parallel quartz veins, crosscutting quartz veins, and *syn*-deformational quartz veins that we attributed to the Cretaceous extensional tectonics described by earlier studies (*e.g.,* Clerc and Lagabrielle, 2014; Abd Elmola et al., 2018; Siron et al., 2020). These structural characteristics suggested multiple episodes of fluid mobility. We collected three main types of quartz-bearing material: (i) proper quartz veins with low abundance of other minerals (n = 4, of which 2 veins may be of Late Variscan origin); (ii) quartz-rich melt veins (leucosomes in migmatites; aplites; pegmatites) of probable Variscan origin (n = 4); (iii) quartz-bearing high-grade rocks (n = 3). The first two types are grouped as quartz-rich veins throughout this manuscript. The veins and high-grade rocks exhibit distinct mineral compositions, which were initially evaluated during field observations (Fig. 2), and further examined with petrographic and quantitative geochemical techniques. Some vein samples yielded inconclusive results and are available in Supplementary Text Table S1 and Supplementary Data Table S4.

For the stepwise crushing of $^{40}Ar/^{39}Ar$, all samples were crushed, washed, sieved, and subjected to standard heavy liquid separation and Frantz isodynamic magnetic separator techniques to obtain pure quartz. In order to separate pure quartz mineral grains with densities of 2.63 g/cm³ and 2.65 g/cm³, heavy liquid densities of 2.62 g/cm³, 2.64 g/cm³, and 2.66 g/cm³ were used. Further purification was required due to the presence of small magnetic minerals. The Frantz isodynamic magnetic separator was set at an electric current of 2 ampere (A) with side slopes of 10°, 5°, 3° and 0°. We used the 2.63 g/cm³ and 2.65 g/cm³ fractions in a final hand-picking step under a binocular microscope. A quantity of 50 mg of quartz mineral grains from each sample, within the size range of 400–500 µm was enclosed in aluminum foil and dispatched to OSU TRIGA reactor for a 12-hour irradiation in the CLICIT facility. Most samples were irradiated with the in-house Drachenfels DRA-2 standard, while the high-grade rocks L.22F (migmatite) and L.24A (charnockite) were irradiated using GA1550 biotite as a standard. For these standards, we applied an intercalibration following Renne et al. (1998) and Kuiper et al. (2008) (for details see Section 3.4.2).

3.2. Fluid inclusion analyses

Fluid inclusion microthermometric measurements undertaken on 250 µm thick sections were performed on an Olympus microscope fitted with a Linkam THMS600 heating-freezing stage and a x100 objective lens at the Department of Earth Sciences, University of Torino. The Linkam stage had an accuracy of ± 0.1 °C for ambient, lower, and higher temperature measurements. Calibration was conducted using pure CO_2 and H_2O fluid inclusions. The salinity, expressed as equivalent weight percent of NaCl, and the density of the fluid inclusions were determined using the FLUID software packages (Bakker, 2003).

Raman analysis of fluid inclusions was carried out with the confocal

LABRAM HR800 (Horiba Jobin Yvon Instruments) at the Department of Earth Sciences, University of Torino. The spectra were collected using an Olympus BX41 microscope and a x100 objective lens. The operating conditions were as follows: emission power of 80 mW, a confocal hole of 200 µm, a slit width of 300 µm, a grating of 600 grooves/mm, and 3–10 accumulations with exposure times of 1–60 seconds each. The calibration was performed using the bands of Si (522 cm⁻¹), of diamond (1332 cm⁻¹) and/or of air N_2 (2331 cm⁻¹). The identification of fluid and solid phases was based on database of reference spectra (Frezzotti et al., 2012). The quantitative composition of the gaseous mixture is expressed in mol% using the method reported by Burke (2001).

3.3. Electron micro probe analyses (EMPA)

The quantitative composition of the mineral chemistry in the vein assemblages, was determined using the JEOL JXA 8530F Hyperprobe at Utrecht University. The operating conditions during analyses were set to an accelerating voltage of 15 kV, a beam current of 10nA, with a beam spot size of 10 µm. The mineral standardization was done by utilizing a suite of reference materials (*e.g.,* synthetic $KTiPO_5$, natural diopside and jadeite). Samples L.17A and L.58A were prepared as polished thin sections, followed by a comprehensive mineralogical observation to ascertain the identification of the minerals before the analysis.

3.4. Analysis of $^{40}Ar/^{39}Ar$ data from stepwise crushing

3.4.1. $^{40}Ar/^{39}Ar$ geochronology

Irradiated samples were measured on a ThermoFisher Helix MC plus mass spectrometer in the Geochronology laboratory at the VUA (Vrije Universiteit Amsterdam). Single grains of the DRA-2 or GA1550 standard were loaded in a copper tray with 3 mm depth holes and heated under high vacuum to 250 °C overnight to clean them from any volatile contamination. A second overnight heating step was performed at 120 °C including the sample chamber, extraction line, and getters to further clean the system from any air contamination. A transparent ZnS cover glass covers the sample holder. A focused *ca.* 5 W laser beam delivered by a water cooled 50 W Synrad CO_2 laser was used for flux monitor single grain total fusion analyses to derive J values for the crushing experiments ranging from 0.003217 to 0.003490. The purification of the released gas was achieved using a cold trap at −70 °C, a Ti getter (400 °C) and hot ST172 and NP10 getters that retain all reactive volatiles and allow only clean argon gas to enter the spectrometer. Argon isotopes of the standards were measured on the H2-L2 collectors where for H2 (m/e40) and H1 (m/e39) Faraday cups 10¹³-ohm amplifiers are used and for AX (m/e38), L1 (m/e37) and L2 (m/e36) compact discrete dynode amplifiers (CDDs) are used. Line blanks were measured every two to four unknowns and were subtracted from succeeding sample data.

About 25–30 mg of quartz is loaded in the crusher tube, the pestle is added carefully with the tube in horizontal position. The crusher is then connected to the extraction line, pumped, and baked overnight at 250 °C. Flexible tubing, valves that connect the crusher to the extraction line are baked at 120 °C. The samples are then crushed by repeatedly lifting and dropping the pestle using an external electromagnet with a frequency of one time per second (1 Hz) controlled by an adjustable power supply and pulse generator. Additional details regarding instrument settings, background corrections, and blank measurements are provided in the Supplementary Texts A1 and A2.

3.4.2. Data processing

Mass discrimination, neutron interference, decay and gain corrections to both samples and standards were applied. Gain calibration is done by correcting for gain relative to the beam intensity as measured on the AX-CDD, using measurements of ~50 fA (m/e 40 ion beam) pipettes of air on each cup and mass discrimination corrections were done measuring a series ~400 fA air pipettes roughly every 12 h. Raw data were processed using the ArArCALC software (Koppers, 2002). For more

in-depth data evaluation, the data processing and visualization software package WebArAr (https://github.com/wuyangchn/webarar, coded by Yang Wu) was used. The apparent ages of vein samples were calculated relative to Drachenfels sanidine (25.552 ± 0.078 Ma; Wijbrans et al., 1995), recalibrated relative with the Fish Canyon Tuff age of 28.201 ± 0.023 Ma (Kuiper et al., 2008). Quartz from high-grade rock samples L.22F and L.24A used GA1550 biotite as standard with an age of 99.44 ± 0.13 Ma, recalculated relative to Kuiper et al. (2008) in combination with the $(^{40}Ar^*/^{39}Ar_K)_{GA1550}/(^{40}Ar^*/^{39}Ar_K)_{FC}$ from Renne et al. (1998).

Decay constants recommended by Min et al. (2000) are used. Sample intensities are normalized to an atmospheric $^{40}Ar/^{36}Ar$ ratio of 298.56 ± 0.31 (Lee et al., 2006) using a discrimination factor that is derived from repeated measurement of aliquots of air argon obtained from a reservoir containing precleaned air argon. All errors in the age results are quoted at the 2σ level and include all the analytical errors.

4. Results

4.1. Mineral compositions in quartz veins

Here we only report mineral compositions from quartz vein samples L.17A and L.58A, which were used for fluid inclusion studies. The rock types and mineral assemblages of all samples are provided in Table 1. Vein L.17A (Fig. 3a & b; Fig. 4a) consists of quartz, Fe-chlorite (chamosite), Fe-biotite, muscovite, and minor apatite. By contrast, the vein sample L.58A (Fig. 3a; Fig. 4b) only contains quartz and Fe-chlorite (chamosite). Representative analytical data for mineral chemistry results are available in the Supplementary Data Table S2.

The XMg ratios, *i.e.*, Mg / (Mg + Fe), of Fe-chlorite in sample L.17A vary from 0.31 to 0.48, with an average of 0.41 (n = 28). In comparison, sample L.58A shows XMg values ranging from 0.37 to 0.49 (n = 2).

In sample L.17A, mica-group minerals exhibit variations in XMg ratios: muscovite ranges from 0.21 to 0.41 (average of 0.33; n = 35), and biotite from 0.34 to 0.41 (average of 0.39; n = 33). All mica analyses show TiO_2 contents below 1 wt%.

4.2. Intracrystalline deformation and fluid infiltration of the high-grade rocks

Quartz in some samples that record Variscan metamorphism shows more complex textures. The quartz in the migmatite L.22F (Fig. 5a) occurs as elongated ribbons with lobate grain boundaries. The quartz ribbons are crosscut by fractures that developed during cooling. These fractures partially healed, resulting in the formation of secondary inclusion trails (Roedder, 1984). The charnockite sample L.24A (Fig. 5b) contains quartz crystals with irregular checkerboard extinction patterns. Quartz grains in the charnockite are crosscut by secondary fluid inclusion trails, pointing towards fluid infiltration after the melts had fully crystallized. Finally, the metagranodiorite sample L.45A (Fig. 5c) exhibits elongated quartz ribbons that have experienced significant recrystallization via sub-grain rotation (SGR).

4.3. Characteristics of fluid inclusions

Samples L.17A (Bélesta) and L.58A (Souanyes) were selected for fluid inclusion microthermometry and Raman analysis for molecular composition of the volatiles in the fluid inclusions. The fluid inclusions in quartz of L.17A are aqueous-carbonic multi-phase inclusions (Fig. 6a) showing evidence for a primary distribution (Roedder, 1984). These inclusions are characterized by their small size (<12 μm in diameter) and consist of liquid water + gaseous phase ± a cubic salt ± carbonates such as calcite and siderite, as determined by their Raman spectra (Fig. 7a & b), *e.g.*, by their peaks at 285 and 1085 cm^{-1} and at 194, 301, 736, and 1090 cm^{-1}, respectively (*e.g.,* Frezzotti et al., 2012). These fluid inclusions displayed metastable behavior (*e.g.,* lacking salt renucleation after melting) or underwent post-trapping modifications (*e. g.,* salt precipitation after cooling) during microthermometric measurements. These phenomena hinder the possibility to acquire an accurate estimate of both the final melting temperatures of hydrohalite and the total homogenization temperatures. Additionally, the lack of freezing of the gaseous phase during cooling provides evidence for the presence of a contaminant gas admixture (specifically N_2, as identified by the Raman peak at 2330 cm^{-1}) within the CO_2 (identified by the Fermi doublet at 1285 and 1388 cm^{-1}). The molar fractions of N_2 and

Table 1
Paragenetic and textural information based on petrographic observations for samples.

| Sample number	Rock type (Vein/Host)	Lithology	Paragenesis	Textural information	Notes
L.32A	Deformed granite vein	Qtz, Bt, Ms, Chl, Kfs (perthitic), Plg (inclusions)	Magmatic origin, Bt and Ms crystallized late in the magmatic sequence	Deformed granitic vein, retrograde mylonite	Qtz shows dynamic recrystallization, strain localized during retrogression
L.21A	Mylonitized leucosome	Qtz, Grt, Kfs, Plg, Ms, Chl	Qtz, Kfs, Plg crystallized from melt but later experienced ductile deformation	Syn- to late-tectonic migmatitic vein (leucosome)	Crystallization from melt during migmatization
L.58A(I)	Qtz-rich vein	Qtz, Chl	Hydrothermal fluid infiltration	Lack of deformation	Chl suggests fluid overprint
L.38C	Mylonitized aplite vein	Qtz, Akfs, Plg, Ms	Qtz underwent dynamic recrystallization into fine-grained aggregates	Ductile deformation, greenschist facies	Quartz dynamically recrystallized
L.38D	Qtz-Tur-rich vein	Qtz, Tur (dravite-schorl), Plg, Ms, Apt, Bt, Epi	Qtz-Tur-rich vein crosscuts the deformed granite indicating it is younger and undeformed	Crosscuts vein; undeformed	Qtz-rich vein with black core, post-deformation
L.17A	Qtz-rich vein	Qtz, Bt, Ms, Chl	Recrystallized during early deformation	Recrystallization in zones of intense deformation	Ductile grain-size reduction and later brittle fractures
L.39A	Pegmatite vein	Akfs (perthitic), Plg (zoned), Qtz, Ms, green Bt	Interstitial Qtz, Ms, green Bt, crystallized from residual eutectic melt	Late-stage eutectic melt products	Late-stage crystallization in a low deformation setting
L.2A(II)	Qtz-rich vein	Qtz, Bt, Opq	Quartz underwent post-crystallization strain	Recrystallization during moderate greenschist facies deformation	–
L.45A	Metagranodiorite	Fsp Qtz, Epi, Amph, Apt, Scap, Ms	High-temperature recrystallization	Strongly deformed and retrogressed	Scapolite porphyroclasts
L.22F	Migmatite	Qtz, Kfs, Crd, Sil, Bt	Qtz and Sil crystallized during high-temperature metamorphism	Fractures crosscutting quartz with Fe-clays	Fe-(oxy) hydroxides indicate late-stage fluid infiltration
L.24A	Charnockite	Qtz, Kfs, Bt, Opx, Grt	Interstitial Qtz and Bt, late crystallization from a melt	High-temperature crystal plastic deformation	Brittle fractures in Grt and Qtz – post crystallization strain
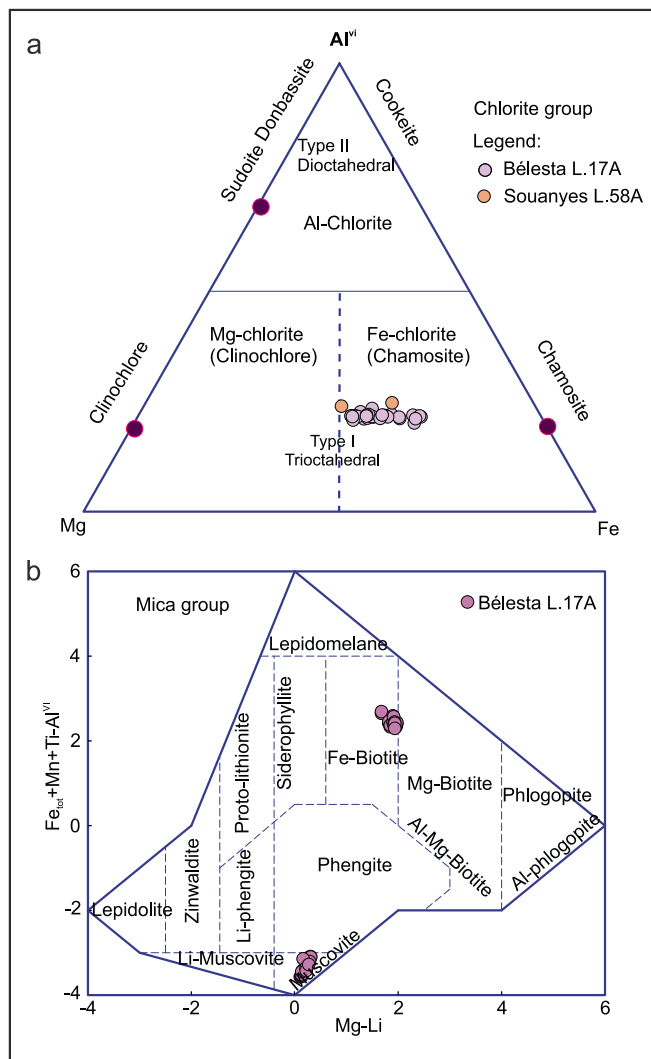
Fig. 3. Chlorite classification diagram (after Wiewióra and Weiss, 1990) in 3a; and Mica classification diagram (Tischendorf et al., 1997) in 3b. Note that Li has not been measured and is assumed to be 0.

CO_2 (Fig. 7c & d) were determined to be 0.27 and 0.73, respectively. Analytical data for Raman analysis are available in the Supplementary Data Table S3.

By contrast, sample L.58A (Souanyes) contains primary two-phase aqueous fluid inclusions (2 to 10 μm in diameter) (Fig. 6b). During microthermometric measurements (Fig. 6c & d), the first liquid phase is visible at temperatures (T_{fm}) ranging from −46 °C to −26 °C, with a peak around −35 °C. This occurrence is attributed to the very small dimension of some fluid inclusions, which prevents the precise determination of the eutectic temperature. Hydrohalite is the last phase to undergo melting at temperatures (T_{mHh}) ranging from −7.0 °C to −0.8 °C. Homogenization always occurs into the liquid phase at temperatures (T_{hL}) from 204.5 °C to 367.7 °C. The bimodal distribution of the asymmetric T_{hL} histogram for sample L.58A (Fig. 6d) reveals the coexistence of modified and preserved fluid inclusions which respectively define a main peak at around 260 °C and a minor peak at around 340 °C. Our data show that the fluid is a brine with a salinity of 25.7 wt% $NaCl_{eq}$.

4.4. Geochronology by stepwise crushing

Neutron-produced $^{37}Ar_{Ca}$, $^{38}Ar_{Cl}$ and $^{39}Ar_K$ can be used as proxies for the chemical concentrations of Ca, Cl and K, respectively, while the ^{40}Ar and ^{36}Ar components shed light on the sources of non-radiogenic argon.

Here we used classic inverse isochrons (*e.g.,* Roddick et al., 1980), for age calculation and three isotope correlation diagrams to document chemical variation in terms of $^{37}Ar_{Ca}$, $^{38}Ar_{Cl}$ and $^{39}Ar_K$.

The total measured ^{40}Ar consists of atmospheric argon ($^{40}Ar_{atm}$), radiogenic ^{40}Ar ($^{40}Ar_R$) derived from in-situ ^{40}K radioactive decay, $^{40}Ar_K$ produced by neutron activation of K and potential excess argon ($^{40}Ar_E$) including inherited argon. Lanphere and Dalrymple (1976) were among the first in reporting the presence $^{40}Ar_E$ revealed by the $^{40}Ar/^{39}Ar$ age spectrum diagrams. It is identified when initial $^{40}Ar/^{36}Ar$ ratios in inverse isochrons exceed the atmospheric standard of 298.56 (Lee et al., 2006).

Clarifying these definitions is crucial for interpreting $^{40}Ar/^{39}Ar$ data. Excess argon ($^{40}Ar_E$) is incorporated into a mineral or rock from external sources, such as entrapped mantle or crustal fluids and is separated from its parent ^{40}K either by high-temperature diffusion or mineral re-equilibration processes (external from system). Inherited argon refers to ^{40}Ar that is introduced into a rock or mineral through physical contamination from older materials or incompletely reset domains in metamorphic rocks (*e.g.,* internal from system; McDougall and Harrison, 1999; Kelley, 2002).

Initial $^{40}Ar/^{36}Ar$ ratios were derived from inverse isochron plots ($^{36}Ar/^{40}Ar$ vs. $^{39}Ar/^{40}Ar$) using isochemical and consecutive step data. For plots with negative slopes and initial $^{40}Ar/^{36}Ar$ values higher than the atmospheric ratio, these values were used to correct the apparent ages of the corresponding segments from which they were derived.

In cases, where the regression produced an initial $^{40}Ar/^{36}Ar$ ratio of less than 298.56, this likely indicates mixing of isotopic contributions. Such mixing can occur between radiogenic argon components from different generation of fluid or solid phases and atmospheric argon, either entrapped in the sample or introduced during stepwise crushing. This scenario aligns with the conceptual model provided by Bai et al. (2013, 2018), demonstrating that stepwise crushing liberates gas from several fluid inclusion generations with partial overlap that can lead to isotopic mixing resulting in reduced the initial $^{40}Ar/^{36}Ar$ ratios.

Bai et al. (2018) demonstrated that even if mixing reduces the initial $^{40}Ar/^{36}Ar$ intercept ratios below 298.56, the maximum apparent ages obtained by the inverse isochron plots can remain geologically significant. Their study showed that mixed gas from primary and secondary fluid inclusions in quartz yielded ages that correspond to apparent ages of coexisting K-feldspar, sericite, and muscovite, while the initial $^{40}Ar/^{36}Ar$ ratio was lower than that of the modern atmosphere. This offers scientific proof for the hypothesis that the apparent ages, under such conditions, still date geological events.

The age spectra, inverse isochrons, release patterns, and three isotope correlation diagrams are used for the data interpretation (Fig. 8a–c; Supplementary Figs. S1–1 & S1–2). All relevant analytical data for age calculations can be found in Table 2.

The release pattern of $^{40}Ar_R$, $^{36}Ar_{atm}$, $^{38}Ar_{Cl}$, $^{39}Ar_K$, and $^{37}Ar_{Ca}$ (Fig. 8c) in the stepwise crushing shows the following characteristics: 1) substantial amounts of $^{40}Ar_R$, $^{36}Ar_{atm}$, $^{38}Ar_{Cl}$, in the fluid during the initial steps. 2) the intermediate stages of crushing exhibit a reduced presence of these gases in comparison to significant concentrations of $^{39}Ar_K$ and $^{37}Ar_{Ca}$. 3) in the final steps, all signals dropped and are distributed evenly (discussed in Section 5.3).

Two quartz-rich melt vein samples (L.32A and L.21A), along with one high-grade metamorphic rock sample from a metagranodiorite L.45A reveal evidence for two distinct episodes of fluid mobility. Based on origin of the quartz-bearing samples, we classify the maximum apparent ages from the final crushing steps into three distinct groups:

4.4.1. Geochronology of quartz-rich veins

The quartz exhibits decreasing apparent ages to a value around ~114 Ma (L.58A(I); Souanyes), ~107 Ma, (L.2A(II); Força Real), ~62 Ma (L.17A; Bélesta), and ~60 Ma (L.38D; Retenue de Vinça). The inverse isochrons for the final crushing steps of L.58A(I), L.2A(II), L.17A, and L.38D are interpreted as maximum apparent ages of 118 ± 8 Ma
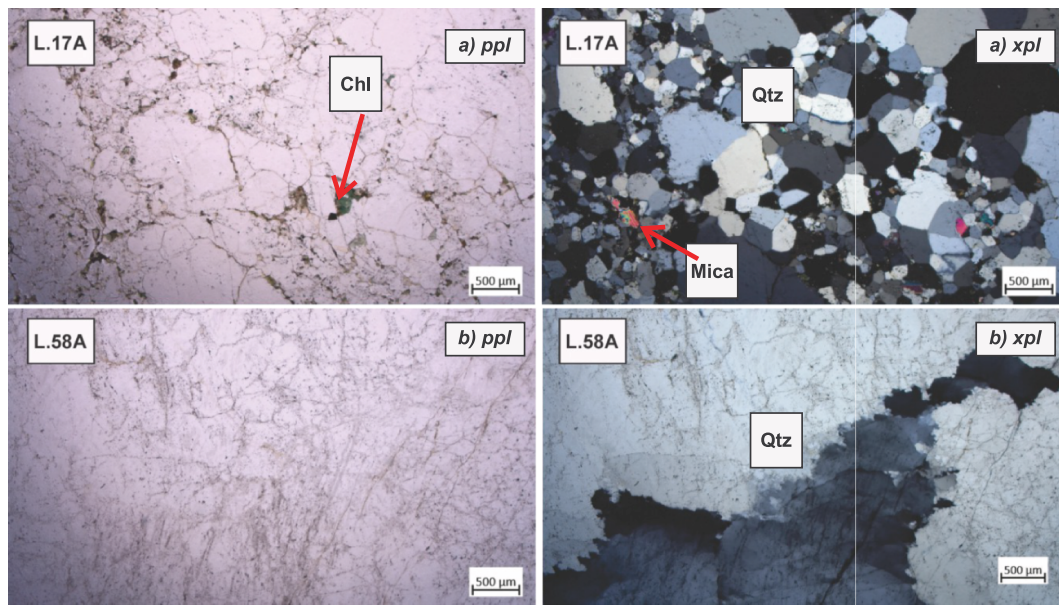
Fig. 4. (**a**) Sample L.17A showing recrystallisation of quartz indicative of multiple episodes of fluid infiltration and deformation, with microcrystalline mica (cross-polarized light) and a chlorite crystal (plane-polarized light). (**b**) Quartz in L.58A exhibiting primary growth textures, suggesting minimal deformation.

($^{40}Ar/^{36}Ar = 300 \pm 7$), 101 ± 8 Ma ($^{40}Ar/^{36}Ar$ ratio $= 303 \pm 8$), 140 ± 11 Ma ($^{40}Ar/^{36}Ar = 293 \pm 8$), and 60.3 ± 1.2 Ma ($^{40}Ar/^{36}Ar = 302 \pm 4$). The maximum apparent ages correspond to the inverse isochron plots, as shown in the age spectra: 118 ± 5 Ma (L.58A(I); MSWD = 6.1; mean square of weighted deviates), 101 ± 2 Ma (L.2A(II); MSWD = 0.5), 139 ± 6 Ma (L.17A; MSWD = 1.3), and 60.1 ± 0.7 Ma (L.38D; MSWD = 3.0).

4.4.2. Geochronology of quartz-rich melt veins

Samples L.39A (Retenue de Vinça), L.21A (Caramany), L.32A (Lansac), and L.38C (Retenue de Vinça) show similar decreasing apparent ages of ~94 Ma, ~87 Ma, ~85 Ma, and ~71 Ma, respectively, in the final crushing steps. Samples L.39A, L.21A, L.32A, and L.38C have inverse isochrons that yield maximum apparent ages of 124 ± 4 Ma ($^{40}Ar/^{36}Ar = 265 \pm 7$), 96 ± 3 Ma ($^{40}Ar/^{36}Ar = 272 \pm 14$), 144 ± 5 Ma ($^{40}Ar/^{36}Ar = 248 \pm 8$), and 70 ± 6 Ma ($^{40}Ar/^{36}Ar = 305 \pm 3$), respectively. The maximum apparent ages identified from the age spectra are 124 ± 2 Ma (L.39A; MSWD = 1.0), 97 ± 2 Ma (L.21A; MSWD = 4.3), 143 ± 2 Ma (L.32A; MSWD = 2.9), and 69 ± 3 Ma (L.38C; MSWD = 2.5).

Additionally, L.32A and L.21A show a secondary line segment in the inverse isochron plot, which yields maximum apparent ages of 81 ± 17 Ma ($^{40}Ar/^{36}Ar = 870 \pm 76$) and 72 ± 5 Ma ($^{40}Ar/^{36}Ar = 762 \pm 34$), respectively. The maximum apparent ages of L.32A and L.21A were recalculated as 81 ± 6 Ma (MSWD = 1.4) and 72 ± 3 Ma (MSWD = 4.9), respectively.

4.4.3. Geochronology of high-grade rocks

Quartz minerals from metagranodiorite (L.45A; Château de Cuxous), charnockite (L.24A; Ansignan), and migmatite (L.22F; Caramany) exhibit excess ^{40}Ar dominated apparent ages in the initial crushing steps, which decrease toward ~110 Ma, ~57 Ma, and ~54 Ma. The final crushing steps in the inverse isochron plot for samples L.45A, L.24A, and L.22F correspond to maximum apparent ages of 119 ± 2 Ma ($^{40}Ar/^{36}Ar$ ratio $= 305 \pm 11$), 61 ± 5 Ma ($^{40}Ar/^{36}Ar$ ratio $= 297 \pm 4$), and 55 ± 3 Ma ($^{40}Ar/^{36}Ar$ ratio $= 300 \pm 4$). The age spectra for the samples L.45A, L.24A, and L.22F in these crushing steps yield maximum apparent ages of 119 ± 1 Ma (MSWD = 1.2), 61 ± 1 Ma (MSWD = 0.6), and 54 ± 1 Ma (MSWD = 0.8), respectively.

In addition, the inverse isochron diagram of L.45A in Château de Cuxous shows a secondary line segment that yields a maximum apparent age of 58 ± 11 Ma with a $^{40}Ar/^{36}Ar$ ratio of 1910 ± 118. Recalculation of this segment yields a maximum apparent age of 58 ± 4 Ma (MSWD = 0.7).

5. Discussion

5.1. Fluid composition of the veins

The chemical compositions and temperatures of the trapped fluids can be determined through fluid inclusion analyses. Phase transitions of solids and liquids in fluid inclusions during heating-freezing experiments provide information on the fluid chemistry. Hydrohalite melting observed in quartz vein fluid inclusions in sample L.58A suggests that the brine primarily contains Na^+ and Cl^- as the dominant dissolved cations and anions (Fontes and Matray, 1993; Hanor, 1994). The temperature of first melting (T_{fm}) of approximately -40 °C suggests the additional presence of dissolved Ca^{2+} ions and the peak melting temperatures around -35 °C may be associated with the presence of additional Fe^{2+} ions (and potentially Mg^{2+}) (Roedder, 1984). The presence of Fe-chlorite and siderite mineral inclusions in the quartz veins, provides additional evidence that the fluids forming the quartz veins contained Fe, Al, and Si species along with H_2O. Similarly, the occurrence of K-Fe phyllosilicates and apatite in the vein mineral assemblages of L.17A indicates the presence of dissolved K^+, Fe^{2+}, and Ca^{2+} cations as well as silicic acid and phosphates anions in the fluid.

The post-trapping evolution of the fluid inclusions is recorded in sample L.58A. The prominent lower-temperature peak (Fig. 6d) suggests that most fluid inclusions experienced post-trapping modifications, leading to a moderate density increase (ca. 1.0 g/cm^3). This increase is likely due to re-equilibration through volume reduction (e.g., plastic deformation or necking down), consistent with isobaric cooling (Bodnar, 2003). In contrast, the peak at higher T_{hL} (340 °C) indicates a significant number of fluid inclusions have preserved their original density (ca. 0.9 g/cm^3) and remain unmodified. The P-T evolution of the host rock is characterized by isobaric cooling, as indicated by the post-trapping modification of some fluid inclusions. Nonetheless, this process did not entirely re-equilibrate all inclusions, since many continue to exhibit their original density.

A fluid salinity of 25.7 wt% $NaCl_{eq}$ obtained from fluid inclusion analysis in L.58A suggests a brine-derived fluid source. Similarly, in sample L.17A, the preservation of cubic salt crystals in the fluid
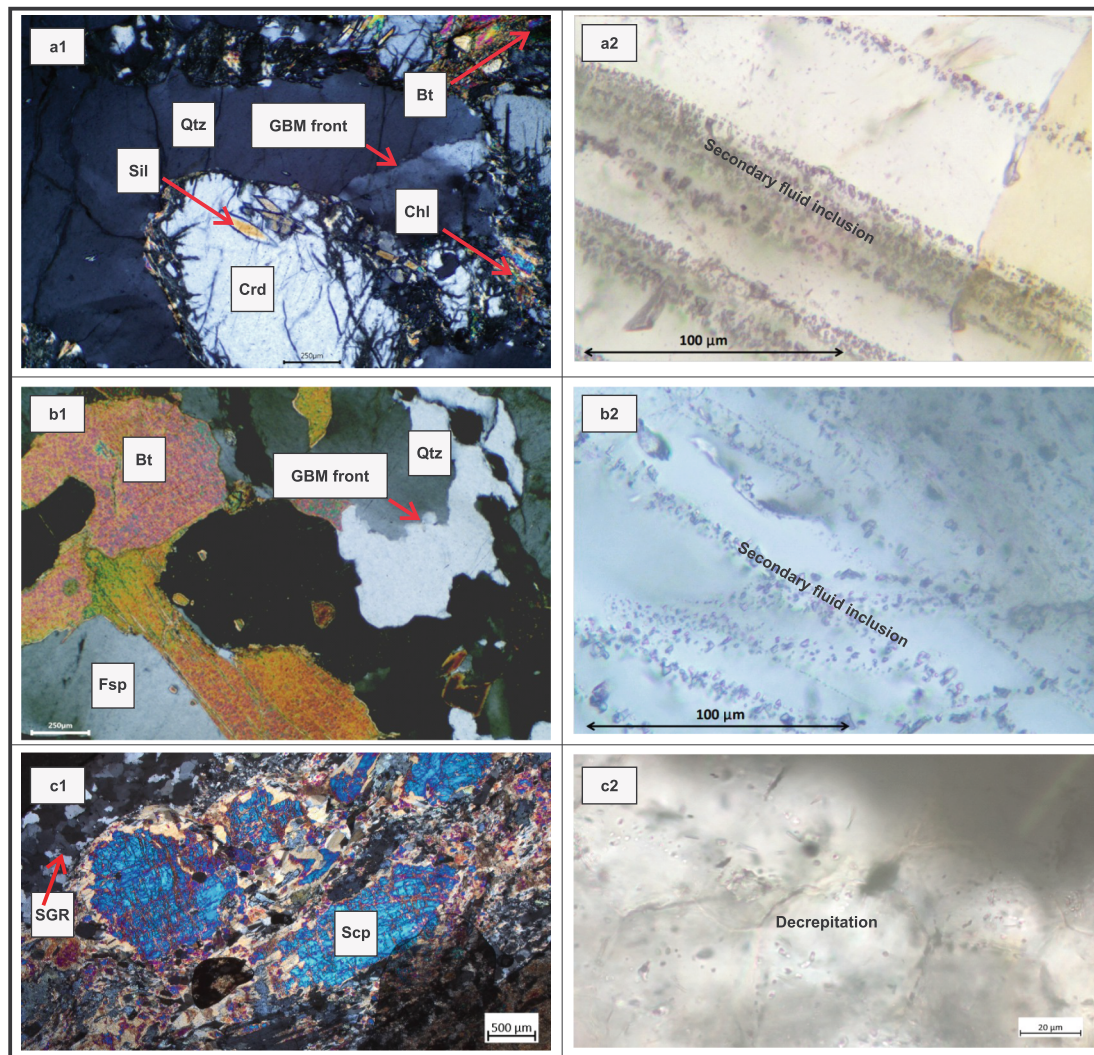
Fig. 5. (**a1**) Migmatite in L.22F, quartz comprises large ribbon-like grains (200–600 μm). The grains show undulose extinction and are crosscut by fractures. Many fractures contain clays and Fe-(oxy)hydroxides, which give them a yellowish to brownish colour. The yellow alteration associated with cordierite is pinite. Cordierite also commonly contains sillimanite inclusions. (**a2**) Secondary fluid inclusion trails and occasionally accompanied by chlorite. (**b1**) Charnockite in L.24A contains a large ribbon of quartz (150–400 μm). Some of the grain boundary migration (GBM) fronts are not smooth but serrated, due to the presence of fine grains (<10 μm) along these boundaries. The serrated texture of GBM and the presence of fine grains suggest overprinting by bulging (BLG) or subgrain rotation recrystallization (SGR), indicating a shift from higher- to lower-temperature deformation conditions. Undulose extinction is also present, suggesting that the quartz experienced subsequent deformation, likely associated with dislocation glide after GBM. (**b2**) Planar structures with secondary fluid inclusions that formed in healed fractures in sample L.24A. (**c1**) Scapolite in L.45A from metagranodiorite appears as large, broken crystals, associated with quartz grains (20–300 μm). The quartz shows subgrain development by SGR. The broken appearance of scapolite suggests it was affected by brittle deformation after crystallization, likely during a later stage of deformation. (**c2**) Decrepitation textures in quartz from L.45A suggest partial fluid loss, resulting in a lower-density remnant of the original fluid.

inclusions implies a salinity higher than the peritectic composition of the H_2O–NaCl system (i.e., >26.3 wt% $NaCl_{eq}$). Direct measurements of K concentrations in these inclusions are unavailable. Therefore, we evaluated whether such high-salinity fluids could plausibly transport quantifiable potassium. Assuming a minimum K/Na ratio based on referenced studies for brines, this would imply the amount of potassium to account for the observed $^{40}Ar^*$ release (discussed in Section 5.2). The interpretation is supported by the three-isotope correlation diagrams (Supplementary Fig. S1–2; $^{37}Ar_{Ca}/^{39}Ar_K$ and $^{38}Ar_{Cl}/^{37}Ar_{Ca}$) and the two-dimensional projection plots (Supplementary Fig. S1–3; apparent age vs. $^{38}Ar_{Cl}/^{39}Ar_K$), which suggest that potassium-bearing fluids were involved during entrapment, and that variations in argon source reservoirs are linked to those apparent ages. The implications of these ratios are discussed in more detail in Section 5.3.

The potassium-bearing fluid likely originated from seawater (*e.g.,* Wickham and Taylor, 1985; Duretz et al., 2019) and became entrapped in marine sediments during early diagenesis. During deep burial and prograde metamorphism, these fluids experienced significant interactions with the surrounding rock and extended thermal alteration, facilitating the decomposition of potassium bearing minerals and the mobilization of dissolved ions. Subsequently, during Early Cretaceous rifting, lithospheric weakening and fault reactivation developed extensional cracks that facilitated the seawater infiltration several kilometres into the crust. The infiltrating seawater mixed with pre-existing metamorphic fluids and interacted with adjacent rocks, resulting in brines richer in Cl^-, Na^+, Ca^{2+}, Mg^{2+}, K^+, Fe^{2+}, SO_4^{2-}, and Zn (Barnes, 1979). These brines subsequently migrated into faults and fractures, leading to quartz vein precipitation.
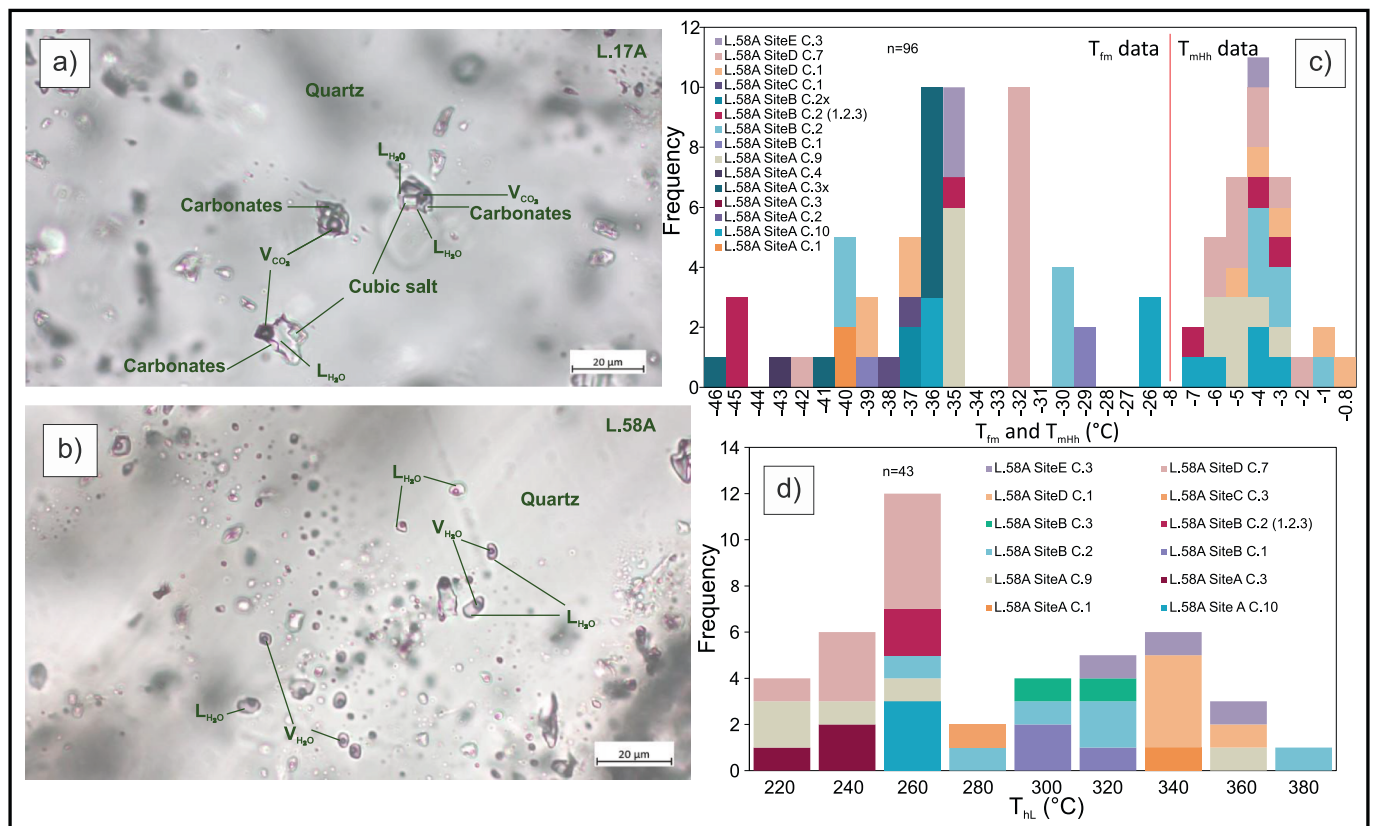
Fig. 6. (**a**) Photomicrographs showing typical fluid inclusion assemblages in the quartz vein of L.17A (Bélesta), consisting of liquid water + gaseous phase ± a cubic salt ± carbonates, with elongated negative crystal shapes and mostly greenish in color. (**b**) Fluid inclusions in L.58A (Souanyes) show more isolated and clustered primary fluid inclusions and are highly transparent. (**c**) Histograms of microthermometric measurements in fluid inclusions from L.58A showing widely dispersed first melting (T_{fm}) temperatures from −46 °C to −26 °C and the hydrohalite melting temperatures (T_{mHh}) ranging between −7 °C to −0.8 °C with a prominent peak at −4 °C. (**d**) Homogenization temperatures into the liquid phase (T_{hL}), measured in fluid inclusions from L.58A, exhibit a bimodal distribution with an asymmetric histogram, suggesting the coexistence of re-equilibrated and preserved fluid inclusions.

5.2. Possible reservoirs of potassium

The potassium content of the quartz in the stepwise crushing analysis is thought to originate predominantly from fluid inclusions (Shi et al., 2018; Hu et al., 2022; Xiao et al., 2022b). Quartz does not accommodate alkali and alkali earth elements such as Na^+, K^+, Mg^{2+}, and Ca^{2+}, into its crystal lattice (Kendrick et al., 2001). Consequently, any detectable amounts of these elements in quartz are attributed to fluid inclusions, which serve as substantial reservoir for such cations (Rossman et al, 1987; Götze et al., 2021). Inherited muscovite inclusions trapped in quartz potentially may influence the potassium budget during stepwise crushing if there is a large age difference between the inherited muscovite and the fluid inclusions. However, the Agly muscovite in the host rock was completely reset during Cretaceous overprinting (Hoogendoorn, 2024). Assuming equal amounts of potassium contents and ages differing by ~50–100 Ma (see Hoogendoorn, 2024 for argon dating of mica; cf. Rauchenstein-Martinek et al., 2016), the resulting observed age would be ~75 Ma and thus would not significantly distort the age spectra as found by the stepwise crushing. Furthermore, the K/Cl release patterns (Supplementary Figs. S1–2 & S1–7) in our data suggest that the observed Ar signal is predominantly influenced by fluid inclusions. Importantly, partition coefficients between minerals and hydrous fluids are extremely low in K-low minerals (*ca.* D ≈ 10^{-6}; Kelley, 2002), resulting in fluid inclusions frequently dominating the radiogenic argon budget. Potassium-bearing fluid inclusions in quartz grains thus represent a potential source for potassium, leading to elevated concentrations of ^{40}K, $^{40}Ar^*$ and $^{39}Ar_K$ (Shi et al., 2018), while the trace muscovite inclusions in quartz crystals do not undermine the interpretation of

fluid-derived Ar. Furthermore, we estimated the recoil losses of ^{39}Ar for our inclusions ranging from 2 to 12 μm in diameter, using recoil distances *ca.* 30 to 50 nm (*e.g.,* Jourdan et al., 2007). These estimations indicate that losses are negligible (≤15% for 2 μm inclusions, ≤6% for 5 μm inclusions, and ≤3% for ≥10 μm inclusions; see the Supplementary Text Table S2).

This hypothesis is supported by the coexistence of quartz and K-bearing minerals such as mica and feldspar in some of the observed quartz veins, which are thought to have recrystallized in the presence of infiltrating, possibly potassium-rich fluid. Although an earlier magmatic fluid may have contributed the potassium content through feldspar breakdown near the solidus, the potassium bearing phases were likely influenced by subsequent deformation and hydrothermal fluid–rock interaction promoting partial recrystallization during Cretaceous rifting. Furthermore, hydrothermal fluids in potassium-rich rocks may account for $^{40}Ar/^{36}Ar$ ratios over 100,000 through the incorporation of radiogenic argon from the previous decay of ^{40}K and released from minerals during fluid–rock interaction at elevated temperature (Snee, 2002; discussed in Section 5.4.1). In addition, the high solubility of the argon in aqueous fluids may increase the ^{40}Ar concentration in these fluids (Kelley, 2002). The potential potassium concentration could be estimated based on fluid inclusion analysis. Assuming ρ = 0.9 g/cm^3 and K/Na ratio of 0.01 as the lowest ratio for brines (Sośnicka et al., 2023; Yu et al., 2023), the potassium concentration in the fluid for sample L.58A is calculated to be ≥ ~2.95 g/L.
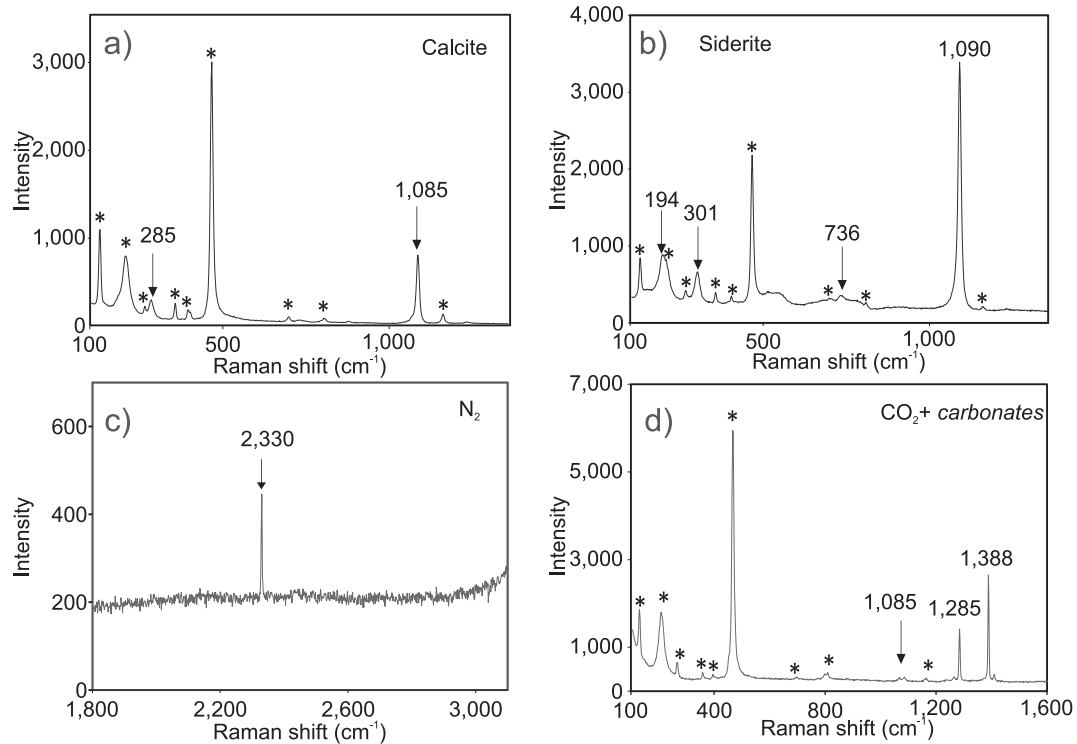
Fig. 7. Raman spectra of the fluid inclusion within the quartz in L.17A (Bélesta) containing (**a–b**) carbonate minerals such as calcite and siderite, and (**c–d**) N_2 and CO_2 + carbonates.

5.3. Fluid chemistry from argon isotopes

The composition of gas released during stepwise crushing in terms of $^{40}Ar_R$, $^{36}Ar_{atm}$, $^{38}Ar_{Cl}$, $^{39}Ar_K$, and $^{37}Ar_{Ca}$ provides constraints on possible fluid sources and the evolution of these fluids during crystallization and/or recrystallization of quartz. In the release pattern (Fig. 8c), a substantial presence of $^{40}Ar_R$, $^{36}Ar_{atm}$, $^{38}Ar_{Cl}$ in the initial crushing steps suggests that the early gas release from the samples is caused by the existence of a gas reservoir with excess ^{40}Ar, as previously discussed (Harrison and McDougall 1980, 1981; Kelley, 2002; Xiao et al., 2019). Such excess ^{40}Ar may have been isolated from its parent ^{40}K by diffusion at high temperatures (Snee, 2002; Bai et al., 2013) or through mineral re-equilibration.

In the intermediate crushing steps (approximately steps ~17–25; Fig. 8a & b; blue segment), samples L.32A, L.21A, and L.45A demonstrate a significant increase in $^{39}Ar_K$ and $^{37}Ar_{Ca}$ accompanied by $^{38}Ar_{Cl}$ signals. The co-release of $^{39}Ar_K$, $^{37}Ar_{Ca}$, and $^{38}Ar_{Cl}$ suggests that K, Ca, and Cl were primarily sourced from Cl-rich secondary fluid inclusions that formed during a later stage of fluid activity (Qiu and Wijbrans, 2006). This geochemical signature indicates the involvement of Cl-bearing hydrothermal fluids, in which Cl⁻ served as dominant complexing ligand that facilitates the transport of cations including Ca^{2+} and K^+ during extended hydrothermal alterations and metamorphic processes (Helgeson and Kirkham, 1976; Stefánsson and Seward, 2004). These fluids may have altered the original K content of the host rocks by dissolving K-bearing phases (Rusk et al, 2004).

During the last stages of crushing (about steps ~45–69; Fig. 8a & b; red segments; see also Supplementary Fig. S1–1) in all samples, the decrease in $^{38}Ar_{Cl}$, along with a continued release of $^{37}Ar_{Ca}$ and $^{39}Ar_K$ indicates a shift from a predominance fluid inclusion to increasing contributions from mineral inclusions. However, the continued, albeit reduced presence of $^{38}Ar_{Cl}$, suggests that Cl-bearing fluid inclusions are still present and continue to contribute to the gas release. This pattern suggests that many reservoirs, including both fluid inclusions and mineral inclusions, may release gas during the final crushing steps, leading

to a mixed release signature (Jiang et al., 2012; Bai et., 2013, 2018; Xiao et al., 2019, 2022a).

A comparative abundance of K, Ca, and Cl concentrations demonstrates differential mixing patterns between different argon components, as shown in Supplementary Fig. S1–2: 1) the K-rich, Cl-poor phase (Fig. S1–2; blue color; Ca/K < 1.0 and Cl/K ≤ 1.0) is defined by comparatively small amounts of Ca and Cl in relation to K. This results in decreased $^{37}Ar_{Ca}/^{39}Ar_K$ and $^{38}Ar_{Cl}/^{37}Ar_{Ca}$ ratios, indicating a K-bearing fluid with little concentrations of Cl and Ca. 2) Cl-rich, K-poor phase (Fig. S1–2; red color; Cl/K > 1.0, irrespective of Ca/K ratios) implies a substantial Cl-bearing fluid component. This results in elevated $^{38}Ar_{Cl}/^{37}Ar_{Ca}$ and $^{37}Ar_{Ca}/^{39}Ar_K$ ratios, indicative of Cl- and Ca-rich fluids and limited contributions of K-bearing phases. 3) Ca-rich, K-poor phase (Fig. S1–2; orange color; Ca/K ≥ 0.1 and Cl/K ≤ 1.0): this phase is characterized by increased Ca in relation to K, accompanied by low chloride concentrations. The elevated $^{37}Ar_{Ca}/^{39}Ar_K$ ratio and decreased $^{38}Ar_{Cl}/^{37}Ar_{Ca}$ ratio indicate a Ca-rich source with minimal chloride impact, potentially suggesting fluid–rock interaction of Ca-rich silicates.

Considering these geochemical characteristics, the correlation between apparent ages and $^{38}Ar_{Cl}/^{39}Ar_K$ offers further distinction regarding argon source reservoirs and argon mobility paths. The graphic presented in Supplementary Fig. S1–3 may facilitate the identification of three primary types of argon reservoirs, based on interpretations from prior studies (Qiu and Jiang, 2007; Qiu and Wijbrans, 2008; Bai et al., 2013, 2018 and 2022): 1) excess argon resulting from deep degassing after the formation of SFIs (secondary fluid inclusions) is often associated with significant scatter data points. 2) excess ^{40}Ar hosted in healed microcracks suggests the redistribution of argon during recrystallization or deformation possibly influenced by variable contributions of Cl-rich fluids. 3) mixtures of SFIs, PFIs (primary fluid inclusions) and solid phases, if present. This indicates overlapping release argon and partial degassing from multiple reservoirs.
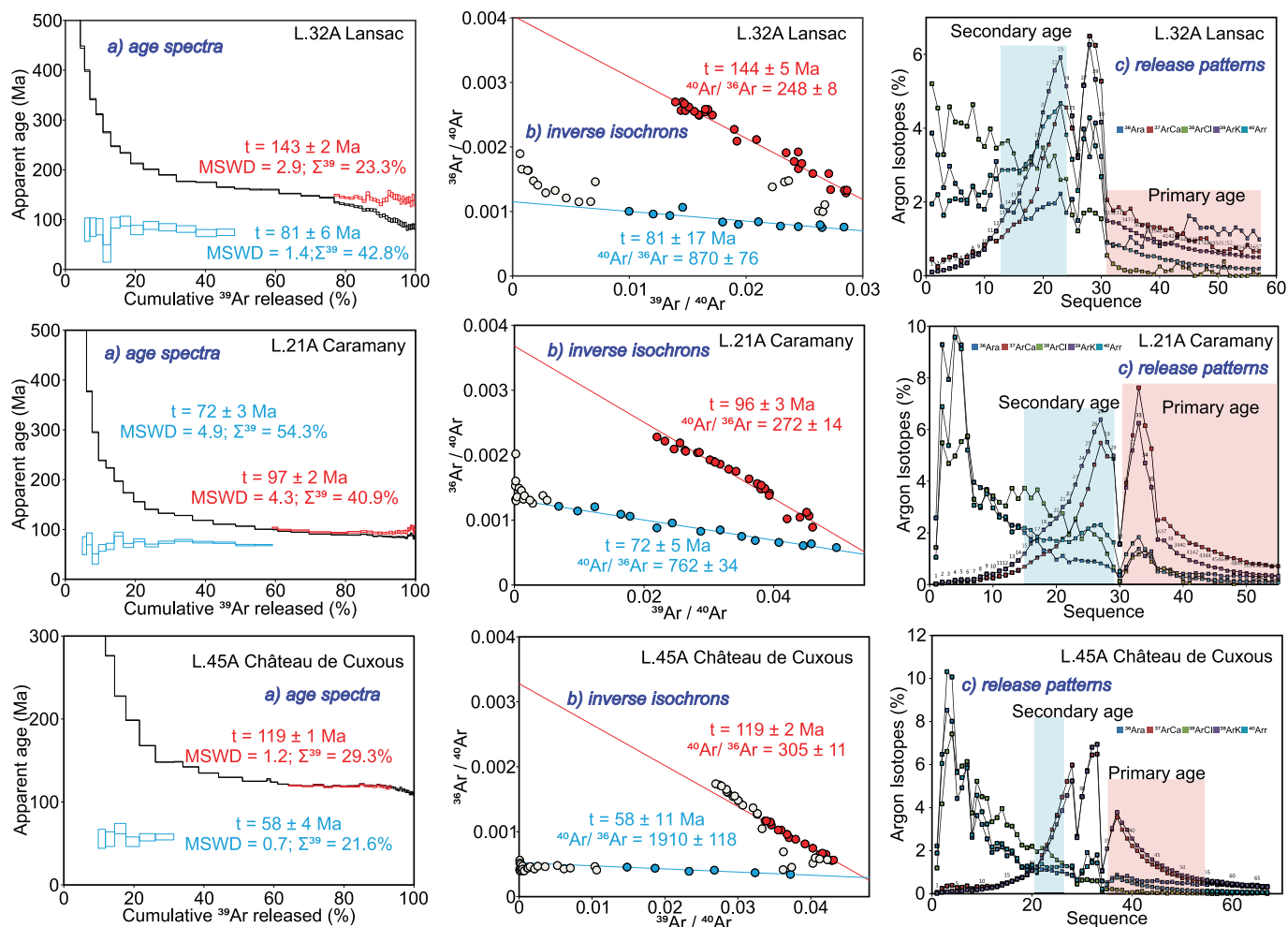
Fig. 8. (a) The $^{40}Ar/^{39}Ar$ age spectra, **(b)** inverse isochron plots, and **(c)** release patterns for the quartz minerals in the Agly Massif and eastern Pyrenees. The dataset comprises quartz-rich vein and high-grade rock samples (L.32A, L.21A, L.45A, L.17A, L.24A, and L.22F). The maximum apparent ages of ~140–90 Ma correspond to partial argon resetting during the peak of Cretaceous tectono–metamorphic activity while apparent ages of ~80–50 Ma are interpreted to indicate fluid infiltration during later stages of exhumation and deformation. More information on the quartz-rich vein samples is provided in the Supplementary Material Fig. S1–1; For detailed data interpretation, see the Discussion section.

5.4. Geochronology by stepwise crushing

The $^{40}Ar/^{39}Ar$ crushing technique yields characteristic gas release patterns that might be related to primary and secondary fluid inclusions (Qiu and Jiang, 2007; Jiang et al., 2012). Generally, it is assumed that argon released from larger, more easily crushed secondary fluid inclusions is measured in the intermediate steps of the crushing experiment, whereas argon derived from smaller, more dispersed primary fluid inclusions is obtained in the final crushing steps (Qiu and Wijbrans, 2006; Xiao et al., 2019, 2022b). Here, given the substantial amounts of excess ^{40}Ar that we consistently observe, we choose to interpret the primary and secondary ages as maximum apparent ages in the context of the regional geological history. The complexity of the system, due to argon being preserved in fluid and solid phases, prevents the determination of plateau and isochron ages which is generally expected for extrusive rocks. Although parameters such as MSWD and the percentage of gas released in the stepwise crushing may be applicable, they are not used to determine accurate crystallization ages. Instead, they provide semi-quantitative information, such as constraining maximum apparent ages and converging sections in the spectra.

5.4.1. Constraints from maximum apparent vein ages

The stepwise crushing $^{40}Ar/^{39}Ar$ analyses of vein quartz from the Agly Massif and surrounding eastern Pyrenees offer new insights into the timing of overprinting processes documented in the quartz veins. Maximum apparent ages of fluid inclusions trapped in quartz veins, derived from the converging sections of stepwise crushing experiments cluster into three groups: *ca.* 140 Ma, 120–90 Ma, and 80–60 Ma. This points to pulsed fluid activity during the inferred peak of the Early Cretaceous tectonic overprinting and subsequent uplift and tectonic unroofing during Late Cretaceous and Paleocene.

Two leucosome samples from Variscan migmatites, L.21A and L.32A, show a negative slope in the inverse isochron plots of the middle crushing steps, suggesting the presence of ^{40}Ar excess component. Correction for this excess argon component lowers the apparent ages from 127 Ma and 205 Ma to 72 Ma and 81 Ma, respectively. These corrected maximum apparent ages point to an association with a period of secondary fluid activity that occurred subsequent to the main phase of quartz crystallization. The high initial $^{40}Ar/^{36}Ar$ ratios (*ca.* 762 ± 34 for L.21A and 870 ± 76 for L.32A) indicate that the late Cretaceous fluids inherited their argon from older reservoirs, either within pre-existing Variscan rocks or from Early Cretaceous lithologies. This argon was probably remobilized through fault reactivation during the Early Cretaceous (Cochelin et al., 2017). Hydrothermal fluid migration along these pathways has been well documented elsewhere in similar meta-morphic–deformation tectonic settings (Turner and Wang, 1992; Allaz
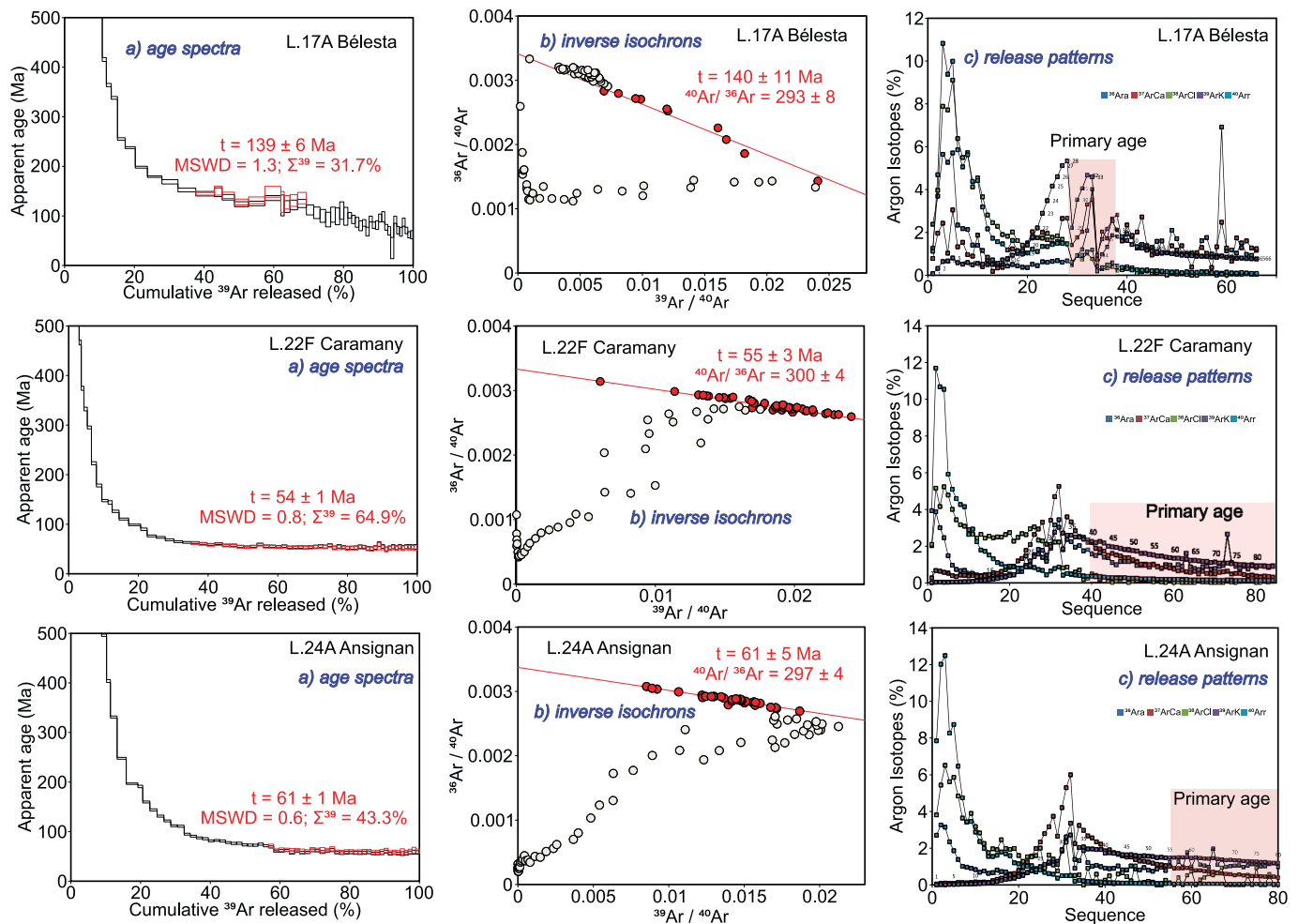
Fig. 8. (*continued*).

Table 2
Summary of maximum apparent ages obtained by $^{40}Ar/^{39}Ar$ stepwise crushing in the Agly Massif and eastern Pyrenees.

Sample number	Locality	Area	Grain size of quartz (μm)	Number of steps	% ^{39}Ar released primary age	Age spectra (Ma)* Primary age of mineralization	Secondary age of mineralization	Inverse isochron age (Ma) Primary age of mineralization	Secondary age of mineralization
L.32A	42°45′39.54″N 2°34′49.04″E	Lansac	150 – 500	57	23.3	143 ± 2	81 ± 6	144 ± 5	81 ± 17
L.21A	42°44′6.82″N 2°34′6.67″E	Caramany	200 – 500	55	40.9	97 ± 2	72 ± 3	96 ± 3	72 ± 5
L.58A(I)	42°33′0.51″N 2°16′1.44″E	Souanyes	400 – 800	49	75.8	118 ± 5	N/A	118 ± 8	N/A
L.38C	42°39′2.82″N 2°30′45.87″E	Retenue de Vinça	300 – 600	73	19.2	69 ± 3	N/A	70 ± 6	N/A
L.38D	42°39′4.51″N 2°30′47.21″E	Retenue de Vinça	50 – 200	77	29.1	60.1 ± 0.7	N/A	60.3 ± 1.2	N/A
L.17A	42°43′20.32″N 2°35′26.55″E	Bélesta	50 – 300	66	31.7	139 ± 6	N/A	140 ± 11	N/A
L.39A	42°39′16.99″N 2°31′37.63″E	Retenue de Vinça	300 – 700	67	14.2	124 ± 2	N/A	124 ± 4	N/A
L.2A(II)	42°43′40.51″N 2°41′49.27″E	Força Real	200 – 800	122	12.7	101 ± 2	N/A	101 ± 8	N/A
L.45A	42°45′8.33″N 2°38′9.49″E	Château de Cuxous	20 – 300	67	29.3	119 ± 1	58 ± 4	119 ± 2	58 ± 11
L.22F	42°44′29.46″N 2°34′40.71″E	Caramany	200 – 600	84	64.9	54 ± 1	N/A	55 ± 3	N/A
L.24A	42°45′11.60″N 2°29′47.28″E	Ansignan	150 – 400	91	43.3	61 ± 1	N/A	61 ± 5	N/A

N/A indicates the data were not available; *The maximum apparent ages in the age spectra were calculated using the non-radiogenic $^{40}Ar/^{36}Ar$ intercept ratio of the isochron regression as the appropriate value for the non-radiogenic end member of the gas mixture.

et al., 2011; Xiao et al., 2019; Hu et al., 2022; Monié et al., 2023). Alternatively, the elevated $^{40}Ar/^{36}Ar$ ratios may indicate the excess radiogenic argon released during the late-Variscan stage, when the crystallization of leucosomes in migmatites near the solidus released hydrous fluids. These fluids may have delivered argon into the system prior to the Cretaceous overprinting.

5.4.2. Maximum apparent ages of the high-grade rocks

Previous dating studies in the Agly Massif (Siron et al., 2020) using U–Th–Pb geochronology have established the following ages (cf. Fig. 9): ~305 Ma for the Ansignan charnockites; ~308 Ma for the Tournefort granodiorite; and ~296–300 Ma for monazites, all indicative of Variscan magmatic processes. In addition, Aumar et al. (2022) reported *syn*-rift Th–U/Pb ages, providing further constraints on the chronology of post-Variscan tectono–metamorphic events. However, $^{40}Ar/^{39}Ar$ and Rb–Sr data on micas and feldspar from the host rocks indicate Cretaceous to late Eocene ages (Albarède et al., 1978; Abd Elmola et al., 2018; Aumar et al., 2022). These findings indicate that the intrusions experienced high-temperature thermal resetting in the Cretaceous Period (*ca.* 92–104 Ma in the east, and 85 Ma in the west), which overprinted the original Variscan U–Pb age signals (*ca.* 296–308 Ma) in these minerals. The resetting is interpreted to have occurred during a Late Mesozoic rifting phase, most likely involving thermal and/or fluid–rock

interactions such as metasomatism and deformation-related recrystallization.

Our stepwise crushing $^{40}Ar/^{39}Ar$ data from fluids trapped in quartz from the high-grade rocks show a wider range of apparent ages from ~120 Ma to ~60–50 Ma. This is consistent with the dataset obtained from biotite crystals of the host rocks using in-situ laser probe analysis for a single sample that yielded 120–90 Ma (Hoogendoorn, 2024). The age spectra and inverse isochron diagrams obtained by stepwise crushing of rock-hosted quartz containing fluid inclusions point to secondary fluid activity during the Early Cretaceous overprinting for sample L.45A and subsequent overprinting in the Early Paleogene for L.22F and L.24A. As an example in L.45A, the final crushing steps (red segment; Fig. 8a & b) yield a maximum apparent age of *ca.* 120 Ma, which points to fluid activity during the Cretaceous high-temperature overprinting. In contrast, the middle crushing steps (~60 Ma; blue segment, Fig. 8a & b) suggest a later phase of secondary fluid infiltration and likely represent post-crystallization processes such as late-stage cooling or isotopic resetting associated with Cenozoic convergence during the Alpine orogeny.

Further evidence for these postulated late pulses of fluid overprinting is provided by petrographic observations on the quartz in the high-grade rocks (Fig. 5a–c). The presence of the textures of lobate grain boundaries in L.22F, as well as pinning, intergranular openings, and dragging microstructures (Fig. 5a), suggest that recrystallization occurred through grain boundary migration recrystallization (GBM) at temperatures above 500 °C. The petrographic features of the charnockite sample L.24A suggest that deformation in quartz crystals took place at temperatures above 500 °C. The interstitial position of quartz grains (Fig. 5b) indicates that they crystalized directly from the charnockitic melt. The crystallization age of the charnockite is approximately 310–300 Ma based on U–Pb geochronology (Vanardois et al., 2022), whereas in metagranodiorite sample L.45A, recrystallization via sub-grain rotation (SGR), points to deformation at temperatures between 400–500 °C. Complete recrystallization to ribbon quartz requires temperatures above 500 °C (*e.g.,* Mainprice et al., 1986; Hirth and Tullis, 1992; Stipp et al., 2002; Bestmann and Prior, 2003; Passchier and Trouw, 2005). Two key implications have been considered:

1. quartz deformation textures indicate solid-state deformation during high-temperature metamorphism and tectonic activity.
2. fluid infiltration occurred after peak deformation and may represent a subsequent hydrothermal overprinting associated with tectonic reactivation.

5.5. Implications for maximum apparent ages by stepwise crushing $^{40}Ar/^{39}Ar$

The maximum apparent ages using $^{40}Ar/^{39}Ar$ stepwise crushing of vein quartz and quartz from high-grade rocks suggest the fluid release occurred in pulses, likely associated with discrete geological events, rather than as a continuous process. These maximum apparent ages are interpreted to reflect the chronology of fluid entrapment. This entrapment could coincide with primary quartz crystallization, recrystallization during Cretaceous tectono–metamorphic overprinting or partial retention of argon during progressive cooling.

The concept of closure temperature for argon diffusion (Dodson, 1973) is not applicable to complex geological systems. In recrystallized quartz, argon retention is influenced not only by diffusion kinetics but also by episodic recrystallization, deformation, and fluid–rock interactions that can reset or disturb the isotopic system (*e.g.,* Verschure et al., 1980; Di Vincenzo et al., 2004; Augier et al., 2005; Beltrando et al., 2009; Villa et al., 2014; Nteme et al., 2023). Moreover, argon loss can occur in an open system, where chemical potential gradients facilitate directed argon flows into these escape pathways including grain boundaries and microcracks.

The apparent ages of *ca.* 140–90 Ma correspond with the peak of the
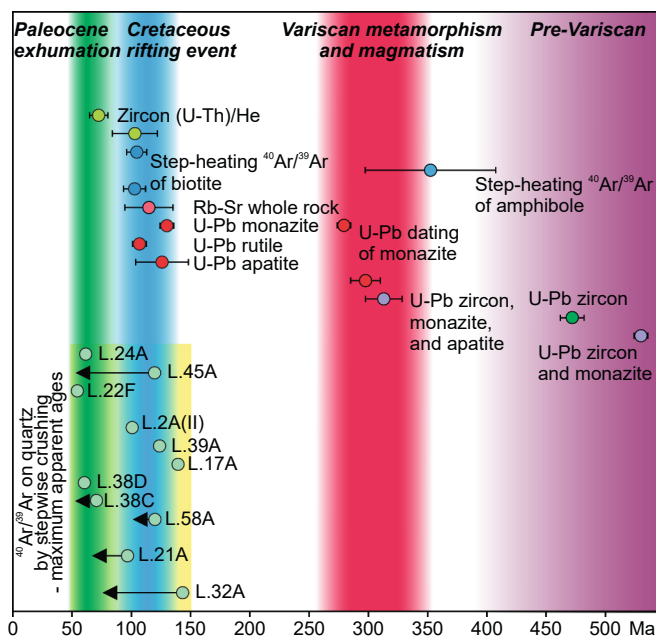
Fig. 9. Summary of the geochronological data from the Agly Massif and eastern Pyrenees, illustrating key thermal and tectonic events from the Neoproterozoic to the Eocene. U–Pb zircon and monazite data constrain the timing of pre-Variscan (*e.g.,* Guille et al., 2019; Odlum and Stockli, 2019; Aumar et al., 2022) and peak Variscan metamorphism and magmatism (*ca.* 305–290 Ma; Respaut and Lancelot, 1983; Olivier et al., 2004, 2008; Poujol et al., 2010; Guille, 2017; Guille et al., 2019; Odlum and Stockli, 2019; Siron et al., 2020; Aumar et al., 2022; Vanardois et al., 2022). Cretaceous tectono–metamorphic overprinting (*ca.* 143–90 Ma; Roubault et al., 1963; Albarède and Michard-Vitrac, 1975; Michard-Vitrac and Allègre, 1975; Odlum and Stockli, 2019; Ternois et al., 2019; Aumar et al., 2022) is recorded by U–Pb apatite, rutile, and monazite, as well as by $^{40}Ar/^{39}Ar$ biotite and whole rock Rb–Sr systems. Our stepwise crushing $^{40}Ar/^{39}Ar$ on quartz further supports this overprint, yielding maximum apparent ages between ~143–90 Ma. Final exhumation during the Paleocene (*ca.* 75–70 Ma) is marked by zircon (U–Th)/He and apatite fission–track ages (Yelland, 1990; Gunnell et al., 2009; Ternois et al., 2019), while stepwise crushing of quartz shows a broader range of apparent ages between ~80–50 Ma. The yellow area shows the results of this study. For samples where the age vector is very short, it overlaps with the datapoint.

Cretaceous tectono-metamorphic event linked to the Caladroy shear zone, interpreted as part of the extensive crustal reworking associated with Early Cretaceous rifting in the Pyrenees region. This rifting phase, documented by extensional structures, metamorphic complexes, and *syn*-rift sedimentation, is thought to have facilitated fluid circulation and increased temperatures, leading to partial argon resetting in quartz-bearing rocks. In contrast, the apparent ages of *ca.* 80–50 Ma are more plausibly associated with episodic fluid infiltration during subsequent phases of exhumation, deformation, and tectonic unroofing. These maximum apparent ages point to intermittent fluid–rock interactions during which the ^{40}Ar-rich fluids were mobilized and subsequently trapped as the system cooled and experienced structural reworking of the massif after the original peak Variscan metamorphism (McCaig 1986; Beaumont et al., 2000; Denèle et al. 2008; Masini et al., 2011; Mouthereau et al., 2014). A compilation of geochronology data, integrating results from this study and previous studies, is shown in Fig. 9.

6. Conclusions

Fluid inclusion analyses and ^{40}Ar/^{39}Ar stepwise crushing results of fluid inclusions hosted in quartz from veins and high-grade rocks from the eastern Pyrenees provide valuable insights into the tecto-no–metamorphic history of the Agly Massif and adjacent areas:

1) The composition of brines in fluid inclusions for samples L.58A and L.17A suggests a seawater-derived origin.
2) The observed ^{37}Ar$_{Ca}$/^{39}Ar$_K$ and ^{38}Ar$_{Cl}$/^{39}Ar$_K$ ratios indicate that the potassium in the fluid inclusions originated from fluids that had previously leached potassium from K-bearing host rocks leading to potassium enrichment relative to fluids initial composition.
3) Evidence from quartz in high-grade rocks, including grain boundary migration and checkerboard extinction patterns, suggests high-temperatures deformation above 500 °C associated with regional metamorphism.
4) Quartz crystallization during rifting and exhumation (*ca.* 140–90 Ma and 80–50 Ma) in veins, coeval recrystallization in older melt veins and high-grade rocks likely resulted from hydrothermal fluid–rock interactions, which promoted mineral growth and/or isotopic resetting.
5) Fluid migration occurred episodically, in discrete pulses over a period of ~90 million years (~140 to 50 Ma). This intermittent fluid mobility, combined with elevated ^{40}Ar/^{36}Ar ratios, indicates fault reactivation throughout the tectonic evolution.

Data availability

Data are available through Zenodo at https://doi.org/10.5281/zeno do.17274411.

CRediT authorship contribution statement

Intan Chalid: Writing – review & editing, Writing – original draft, Visualization, Software, Resources, Investigation, Formal analysis, Data curation. **Jan R. Wijbrans:** Writing – review & editing, Supervision, Resources, Project administration, Methodology, Funding acquisition, Conceptualization. **Yang Wu:** Writing – review & editing, Visualization, Validation, Software, Resources, Data curation, Conceptualization. **Simona Ferrando:** Writing – review & editing, Validation, Resources, Methodology, Formal analysis, Data curation, Conceptualization. **Sander Hoogendoorn:** Writing – review & editing, Investigation, Formal analysis, Conceptualization. **Leo M. Kriegsman:** Writing – review & editing, Validation, Supervision, Resources, Investigation, Formal analysis, Data curation, Conceptualization. **Klaudia F. Kuiper:** Writing – review & editing, Validation, Supervision, Resources, Methodology, Investigation, Formal analysis, Data curation, Conceptualization.

Appendix A. Supplementary material

Supplementary material Text A.1 includes instrument settings, background corrections, and blank measurements; Text A.2 provides correction factors for neutron interference; Table S1 presenting inconclusive age data of vein samples in the Agly Massif and eastern Pyrenees; Table S2 showing ^{39}Ar recoil loss (%) for fluid inclusions; Text B.1 presents petrographic description with additional information from EMPA data; Figure S1–1 presents age spectra, inverse isochron plots, Ar release spectra of conclusive samples; Figure S1–2 illustrates isotope correlation diagram based on Ca/K and Cl/K ratios of conclusive samples; Figure S1–3 depicts correlation diagram between apparent ages and Cl/K ratios; Figure S1–4 displays age spectra and inverse isochron diagrams from inconclusive samples; Figure S1–5 shows K/Ca inconclusive samples; Figure S1–6 presents K/Cl inconclusive samples; Figure S1–7 exhibits the release spectra of K/Ca and K/Cl ratios of conclusive samples. Supplementary material to this article can be found online at https://doi.org/10.1016/j.gca.2025.10.024.

References

Abd Elmola, A., Buatier, M., Monié, P., Labaume, P., Trap, P., Charpentier, D., 2018. ^{40}Ar/^{39}Ar muscovite dating of thrust activity: a case study from the Axial Zone of the Pyrenees. Tectonophysics 745, 412–429.

Albarède, F., Michard-Vitrac, A., 1975. Age and significance of the North Pyrenean metamorphism. Earth Planet. Sci. Lett. 40, 327–332.

Albarède, F., Feraud, G., Kaneoka, I., Allègre, C.J., 1978. ^{39}Ar-^{40}Ar Dating: the importance of k-feldspars on multi-mineral data of polyorogenic areas. J. Geol. 86, 581–598.

Allaz, J., Engi, M., Berger, A., Villa, I.M., 2011. The effects of retrograde reactions and of diffusion on ^{40}Ar–^{39}Ar ages of micas. J. Petrol. 52, 691–716.

Augier, R., Agard, P., Monié, P., Jolivet, L., Robin, C., Booth-Rea, G., 2005. Exhumation, doming and slab retreat in the Betic Cordillera (SE Spain): in situ ^{40}Ar/^{39}Ar ages and P-T-D-t paths for the Nevado-Filabride complex. J. Metam. Geol. 23, 357–381.

Aumar, C., Merle, O., Bosse, V., Monié, P., 2022. Syn-rift cretaceous deformation in the Agly Variscan massif (Eastern Pyrenees, France). Earth Sci. Bull. 193, 6.

Bai, X.-J., Jiang, Y.D., Hu, R., Gu, X.P., Qiu, H., 2018. Revealing mineralization and subsequent hydrothermal events: Insights from ^{40}Ar/^{39} isochron and novel gas mixing lines of hydrothermal quartzs by progressive crushing. Chem. Geol. 483, 332–341.

Bai, X.-J., Liu, M., Hu, R., Fang, Y., Liu, X., Tang, B., Qiu, H., 2022. Well constrained mineralization ages by integrated ^{40}Ar/^{39}Ar and U-Pb dating techniques for the Xitian W-Sn polymetallic deposit, South China. Econ. Geol. 117, 833–852.

Bai, X.-J., Wang, M., Jiang, Y.D., Qiu, H., 2013. Direct dating of tin-tungsten mineralization of the Piaotang Tungsten deposit, South China, by ^{40}Ar/^{39}Ar progressive crushing. Geochim. Cosmochim. Acta 114, 1–12.

Bakker, R.J., 2003. Package FLUIDS 1. Computer programs for analysis of fluid inclusion data and for modelling bulk fluid properties. Chem. Geol. 194, 3–23.

Barbarand, J., Bour, I., Pagel, M., Quesnel, F., Delcambre, B., Dupuis, C., Yans, J., 2018. Post-Paleozoic evolution of the northern Ardennes Massif constrained by apatite fission-track thermochronology and geological data. Bull. Soc. Geol. Fr. 189, 1–16.

Barnes, H.L., 1979. Geochemistry of hydrothermal ore deposits, second ed. Wiley, New York. 798 pp.

Beaumont, C., Muñoz, J.A., Hamilton, J., Fullsack, P., 2000. Factors controlling the Alpine evolution of the central Pyrenees inferred from a comparison of observations and geodynamical models. J. Geophys. Res. Solid Earth 105, 8121–8145.

Beltrando, M., Lister, G.S., Forster, M., Dunlap, W.J., Fraser, G., Hermannet, J., 2009. Dating microstructures by the ^{40}Ar/^{39}Ar step-heating technique: Deformation-pressure-temperature-time history of the Penninic units of the western Alps. Lithos 113, 801–819.

Bestmann, M., Prior, D.J., 2003. Intergranular dynamic recrystallization in naturally deformed calcite marble: Diffusion accommodated grain boundary sliding as a result of subgrain rotation recrystallization. J. Struct. Geol. 10, 1597–1613.

Bodnar, R.J., 2003. Reequilibration of fluid inclusions. Mineral. Assoc. Can. Short Course. 32, 213–230.

Bons, P.D., 2001. The formation of large quartz veins by rapid ascent of fluids in mobile hydrofractures. Tectonophysics 336, 1–17.

BRGM., 2021. Geological Map of France 1:242,000: Coordinate System WGS 1984 Web Mercator (Auxiliary Sphere). https://www.brgm.fr.

Burbank, D.W., Puigdefàbregas, C., Muñoz, J.A., 1992. The chronology of the Eocene tectonic and stratigraphic development of the eastern Pyrenean foreland basin, northeast Spain. GSA Bull. 104, 1101–1120.

Burke, E.A.J., 2001. Raman microspectromety of fluid inclusions. Lithos 55, 139–158.

Clerc, C., Lagabrielle, Y., 2014. Thermal control on the modes of crustal thinning leading to mantle exhumation: Insights from the cretaceous Pyrenean hot paleomargins. Tectonics 33, 1340–1359.

Cochelin, B., Lemirre, B., Denèle, Y., Saint, B.M., Lahfid, A., Duchêne, S., 2017. Structural inheritance in the Central Pyrenees: the Variscan to Alpine tectonometamorphic evolution of the Axial zone. J. Geol. Soc. 175, 336–351.

Denèle, Y., Laumonier, L., Paquette, J.L., Olivier, P., Gleizes, G., Barbey, P., 2014. Timing of granite emplacement, crustal flow and gneiss dome formation in the Variscan segment of the Pyrenees. Geol. Soc. Lond. Spec. Publ. 405, 265–287.

Denèle, Y., Olivier, P., Gleizes, G., 2008. Progressive deformation of a zone of magma transfer in a transpressional regime: the Variscan Mérens shear zone (Pyrenees, France). J. Struct. Geol. 30, 1138–1149.

Denèle, Y., Olivier, P., Gleizes, G., Barbey, P., 2009. Decoupling between the Middle and Upper Crust during Transpression-Related Lateral Flow: Variscan Evolution of the Aston Gneiss Dome (Pyrenees, France). Tectonophysics 477, 244–261.

Di Vincenzo, G., Rocchi, S., Rosetti, F., Storti, F., 2004. ^{40}Ar-^{39}Ar dating of pseudotachylytes: the effect of clast-hosted extraneous argon in Cenozoic fault-generated friction melts from the West Antarctic Rift System. Earth Planet. Sci. Lett. 223, 349–364.

Dodson, M.H., 1973. Closure temperature in cooling geochronological and petrological systems. Contrib. Miner. Petrol. 40, 259–274.

Duretz, T., Asti, R., Lagabrielle, Y., Brun, J.-P., Jourdon, A., Clerc, C., Corre, B., 2019. Numerical modelling of cretaceous Pyrenean rifting: the interaction between mantle exhumation and syn-rift salt tectonics. Basin Res. 31, 363–380.

Fontes, J.C., Matray, J.M., 1993. Geochemistry and origin of formation brines from the Paris Basin. France. Chem. Geol. 109, 177–200.

Ford, M., Hemmer, L., Vacherat, A., Gallagher, K., Christophoul, F., 2016. Retro-wedge foreland basin evolution along the ECORS line, eastern Pyrenees. France. J. Geol. Soc. London 173, 419–437.

Frezzotti, M.L., Tecce, F., Casagli, A., 2012. Raman spectroscopy for fluid inclusion analysis. J. Geochem. Explor. 112, 1–20.

Götze, J., Pan, Y., Müller, A., 2021. Mineralogy and mineral chemistry of quartz: a review. Mineral. Mag. 85, 639–664.

Guille, B.T., 2017. Relation entre magmatisme et métamorphisme Haute-Température Basse-Pression. Réexamen du massif de l'Agly (Pyrénées Orientales). Université Pierre et Marie Curie-Paris VI). Doctoral dissertation.

Guille, B.T., Olivier, P.H., Paquette, J.L., Bosse, V., Guillaume, D., 2019. Evolution of the middle crust of the Pyrenees during the Paleozoic: new data on the plutonic rocks from the North Pyrenean Agly Massif. J. Int. Earth Sci. 108, 245–265.

Gunnell, Y., Calvet, M., Brichau, S., Carter, A., Aguilar, J.P., Zeyen, H., 2009. Low long-term erosion rates in high-energy mountain belts: Insights from thermo-and biochronology in the Eastern Pyrenees. Earth Planet. Sci. Lett. 278, 208–218.

Hanor, J.S., 1994. Origin of saline fluids in sedimentary basins. Geol. Soc. Lond. Spec. Publ. 78, 151–174.

Harrison, T.M., McDougall, I., 1980. Investigations of an intrusive contact, northwest Nelson, New Zealand II. Diffusion of radiogenic and excess ^{40}Ar in biotite and hornblende. Geochim. Cosmochim. Acta 44, 2005–2020.

Harrison, T.M., McDougall, I., 1981. Excess ^{40}Ar in Metamorphic Rocks from Broken Hill, New South Wales - Implications for ^{40}Ar/^{39}Ar Age Spectra and the thermal history of the Region. Earth Planet. Sci. Lett. 55, 123–149.

Helgeson, H.C., Kirkham, D.H., 1976. Theoretical prediction of the thermodynamic properties of aqueous electrolytes at high pressures and temperatures. III Equation of state for aqueous species at infinite dilution. Am. J. Sci. 276, 97–240.

Hirth, G., Tullis, J., 1992. Dislocation creep regimes in quartz aggregates. J. Struct. Geol. 14, 145–159.

Hoogendoorn S. B., 2024. Argon mobility in the mid-lower continental crust: Insights from the Agly Massif and El Hoyazo. *PhD dissertation, Open University, Milton Keynes, UK*, 405 pp. https://oro.open.ac.uk/102127/.

Honegger L., Adatte T., Spangenberg J.E., Poyatos-Moré M., Ortiz A., Ellis C. M., Huyghe D., Puigdefàbregas C., Garcés M., Vinyoles A., Valero L., Läuchli C., Nowak A., Fildani A., Clark, J. D. and Castelltort S., 2021. Tectonics, Climate and Topography: Oxygen stable isotopes and the early Eocene growth of the Pyrenees. *Solid Earth Discuss.* [preprint], https://doi.org/10.5194/se-2021-12, 2021.

Hu, R., Pang, B., Bai, X., Brouwer, F.M., Bai, L., Liu, X., Li, Y., Xu, J., Qiu, H., 2022. Progressive crushing ^{40}Ar/^{39}Ar dating of a gold-bearing quartz vein from the Liaotun Carlin-type gold deposit, Guangxi, southern China. Sci Rep. 12, 12793.

Jiang, Y., Qiu, H., Xu, Y., 2012. Hydrothermal fluids, argon isotopes, and mineralization ages of the Fankou Pb-Zn deposit in south China: Insights from sphalerite ^{40}Ar/^{39}Ar progressive crushing. Geochim. Cosmochim. Acta 84, 369–379.

Jourdan, F., Matzel, J.P., Renne, P.R., 2007. ^{39}Ar and ^{37}Ar recoil loss during neutron irradiation of sanidine and plagioclase. Geochim. Cosmochim. Acta 71, 2791–2808.

Kelley, S., 2002. Excess argon in K-Ar and Ar-Ar geochronology. Chem. Geol. 188, 1–22.

Kendrick, M.A., Burgess, R., Pattrick, R.A.D., Turner, P.G., 2001. Halogen and Ar–Ar age determinations of inclusions within quartz veins from porphyry copper deposits using complementary noble gas extraction techniques. Chem. Geol. 177, 351–370.

Koppers, A.A.P., 2002. ArArCALC—software for ^{40}Ar/^{39}Ar age calculations. Comput. Geosci. 28, 605–619.

Kuiper, K.F., Deino, A., Hilgen, F.J., Krijgsman, W., Renne, P.R., Wijbrans, J.R., 2008. Synchronizing rock clocks of earth history. Science 320, 500–504.

Lagabrielle, Y., Clerc, C., Vauchez, A., Lahfid, A., Labaume, P., Azambre, B., Fourcade, S., Dautria, J.M., 2016. Very high geothermal gradient during mantle exhumation recorded in mylonitic marbles and carbonate breccias from a Mesozoic Pyrenean palaeomargin (Lherz area, North Pyrenean Zone, France). C.R Geosci. 348, 290–300.

Lanphere, M.A., Dalrymple, G.B., 1976. Identification of Excess ^{40}Ar by the ^{40}Ar/^{39}Ar age spectrum technique. Earth Planet. Sci. Lett. 32, 141–148.

Lee, J.Y., Marti, K., Severinghaus, J.P., Kawamura, K., Yoo, H.S., Lee, J.B., Kim, J.S., 2006. A redetermination of the isotopic abundances of atmospheric Ar. Geochim. Cosmochim. Acta 70, 4507–4512.

Mainprice, D., Bouchez, J.L., Blumenfeld, P., Tubia, J.M., 1986. Dominant c-slip in naturally deformed quartz: Implications for dramatic plastic softening at high temperature. Geology 14, 819–822.

Masini, E., Manatschal, G., Mohn, G., Ghienne, J.-F., Lafont, F., 2011. The tectono-sedimentary evolution of a supra-detachment rift basin at a deep-water magma-poor rifted margin: the example of the Samedan Basin preserved in the err nappe in SE Switzerland. Basin Res. 23, 652–677.

Maurel, O., Monié, P., Pik, R., Arnaud, N., Brunel, M., Jolivet, M., 2008. The Meso-Cenozoic thermo-tectonic evolution of the Eastern Pyrenees: an ^{40}Ar/^{39}Ar fission track and (U-Th)/ He thermochronological study of the Canigou and Mont-Louis massifs. J. Int. Earth Sci. 97, 565–584.

McCaig, A., 1986. Thick and thin-skinned tectonics in the Pyrenees. Tectonophysics 129, 319–342.

McDougall, I., Harrison, T.M., 1999. Geochronology and thermochronology by the ^{40}Ar/^{39}Ar method, second ed. Oxford Univ. Press, New York, p. 269.

Mezger, J.E., Gerdes, A., 2014. Early Variscan (Visean) granites in the core of central Pyrenean gneiss domes: implications from laser ablation U-Pb and Th-Pb studies. Gondwana Res. 29, 181–198.

Michard-Vitrac, A., Allègre, C.J., 1975. ^{238}U–^{206}Pb, ^{235}U–^{207}Pb, systematics on Pyrenean basement. Contrib. Mineral. Petrol. 51, 205–212.

Min, K., Mundil, R., Renne, P.R., Ludwig, K.R., 2000. A test for systematic errors in ^{40}Ar/^{39}Ar geochronology through comparison with U/Pb analysis of a 1.1-Ga rhyolite. Geochim. Cosmochim. Acta 64, 73–98.

Monié, P., Münch, P., Milesi, G., Bonno, M., Iemmolo, A., 2023. ^{40}Ar/^{39}Ar geochronology of crustal deformation. Comptes Rendus. Géosci. 356, 1–29.

Mouthereau, F., Filleaudeau, P.-Y., Vacherat, A., Pik, R., Lacombe, O., Fellin, M.G., Castelltort, S., Christophoul, F., Masini, E., 2014. Placing limits to shortening evolution in the Pyrenees: Role of margin architecture and implications for the Iberia/Europe convergence. Tectonics 33, 2283–2314.

Nteme, J., Scaillet, S., Gardés, E., Duval, F., Nabelek, P., Mottolese, A., 2023. Defect-controlled ^{40}Ar diffusion domain structure of white micas from high-resolution ^{40}Ar/^{39}Ar crystal mapping in slowly-cooled muscovite. Geochim. Cosmochim. Acta 342, 84–107.

Odlum, M., Stockli, D.F., 2019. Thermotectonic evolution of the north Pyrenean Agly Massif during early cretaceous hyperextension using multi-mineral U-Pb thermochronometry. Tectonics 38, 1509–1531.

Ogg, J.G., Agterberg, F.P., Gradstein, F.M., 2004. The cretaceous period. In: Smith, A.G. (Ed.), A Geologic Time Scale 2004. Cambridge University Press, Cambridge, p. 589.

Olivetti, V., Balestrieri, M.L., Godard, V., Bellier, O., Gautheron, C., Valla, P.G., Zattin, M., Faccenna, C., Pinna-Jamme, R., Manchuel, K., 2020. Cretaceous and late Cenozoic uplift of a Variscan Massif: the case of the French Massif Central studied through low temperature thermochronometry. Geol. Soc. Am. 12, 133–149.

Olivier, P., Gleizes, G., Paquette, J.L., 2004. Gneiss domes and granite emplacement in an obliquely convergent regime: New interpretation of the Variscan Agly Massif (Eastern Pyrenees, France). Spec. Pap. Geol. Soc. Am. 229–242.

Olivier, P., Gleizes, G., Paquette, J.L., Muñoz, S.C., 2008. Structure and U–Pb dating of the Saint-Arnac pluton and the Ansignan Charnockite Agly Massif.: a cross-section from the upper to the middle crust of the Variscan Eastern Pyrenees. J. Geol. Soc. Lond. 165, 141–152.

Passchier, C.W., Trouw R.A.J., 2005. Microtectonics. *Springer*, 372 pp.

Philpotts A. R and Ague J. J., 2009. Principles of igneous and metamorphic petrology. *The Univ. Press, Cambridge* second ed, 667 pp.

Poitrenaud, T., Poujol, M., Augier, R., Marcoux, E., 2020. The polyphase evolution of a late Variscan W/Au (Salau, French Pyrenees): insights from REE and U/Pb LA-ICP-MS analyses. Mineral. Deposita 55, 1127–1147.

Poujol, M., Boulvais, P., Košler, J., 2010. Regional-scale cretaceous albitization in the Pyrenees: evidence from in situ U-Th-Pb dating of monazite, titanite, and zircon. J. Geol. Soc. 167, 751–767.

Poujol, M., Pitra, P., Van den Driessche, J., Tartèse, R., Ruffet, G., Paquette, J.L., Poilvet, J.C., 2017. Two-stage partial melting during the Variscan extensional tectonics (Montagne Noire, France). J. Int. Earth Sci. 106, 477–500.

Qiu, H.N., Jiang, Y.D., 2007. Sphalerite ^{40}Ar/^{39}Ar progressive crushing and stepwise heating techniques. Earth Planet. Sci. Lett. 256, 224–232.

Qiu, H., Wijbrans, J., 2006. Paleozoic ages and excess [40]Ar in garnets from the Bixiling eclogite in Dabieshan, China: New insights from [40]Ar/[39]Ar dating by stepwise crushing. Geochim. Cosmochim. Acta 70, 2354–2370.

Qiu, H., Wijbrans, J.R., 2008. The Paleozoic metamorphic history of the Central Orogenic Belt of China from [40]Ar/[39]Ar geochronology of eclogite garnet fluid inclusions. Earth Planet. Sci. Lett. 268, 501–514.

Qiu, H., Wu, H., Yun, J., Feng, Z., Xu, Y., Mei, L., Wijbrans, J., 2011. High precision [40]Ar/[39]Ar age of the gas emplacement into Songliao Basin. Geology 39, 451–454.

Rauchenstein-Martinek, K., 2014. Metamorphic fluid history along a cross section through the central Alps: constraints from LA-ICPMS analysis of fluid inclusions and Ar-Ar geochronology. Ph.d. Thesis. ETH Zurich Nr. 2202.

Rauchenstein-Martinek, K., Wagner, T., Walle, M., Heinrich, C.A., Arlt, T., 2016. Chemical evolution of metamorphic fluids in the Central Alps, Switzerland: insight from LA-ICPMS analysis of fluid inclusions. Geofluids 16, 877–908.

Renne, P.R., Swisher, C.C., Deino, A.L., Karner, D.B., Owens, T.L., DePaolo, D.J., 1998. Intercalibration of standards, absolute ages and uncertainties in Ar-[40]/Ar-[39] dating. Chem. Geol. 145, 117–152.

Respaut, J.P., Lancelot, J.R., 1983. U/Pb dating on zircons and monazites of the synmetamorphic emplacement of the Ansignan charnockite (Agly Massif-France). Neues Jahrbuch Für Mineralogie-Abhandlungen 147, 21–34.

Roddick, J.C., Cliff, R.A., Rex, D.C., 1980. The evolution of excess argon in alpine biotites – [40]Ar-[39]Ar analysis. Earth Planet. Sci. Lett. 48, 185–208.

Roedder, E., 1984. Fluid inclusions. Rev. Mineral. 12.

Rosenbaum, G., Lister, G.S., Duboz, C., 2002. Relative motions of Africa, Iberia, and Europe during Alpine orogeny. Tectonophysics 359, 117–129.

Rossman, G.R., Weis, D., Wasserburg, G.J., 1987. Rb, Sr and Sm concentrations in quartz. Geochim. Cosmochim. Acta 51, 2325–2329.

Roubault, M., Leutwein, F., Sonet, J., 1963. Mise en évidence de quatre «âges apparents» dans les massifs granitiques et les séries cristallophylliennes des Pyrénées. Comptes Rendus De L'académie Des Sciences 257, 3786–3789.

Rusk, B.G., Reed, M.H., Dilles, J.H., Klemm, L.M., Heinrich, C.A., 2004. Compositions of magmatic-hydrothermal fluids determined by LA-ICP-MS of fluid inclusions from the porphyry copper–molybdenum deposit at Butte. MT. Chem. Geol. 210, 173–199.

Shi, K., Wang, K., Yu, H., Wang, Z., Ma, X., Bai, X., Wang, R., 2018. The [40]Ar/[39]Ar dating of quartz: new insights into the metallogenic chronology of the Jinchang gold deposit and its geological significance. Sci. Rep. 8, 13879.

Siron, G., Goncalves, P., Marquer, D., Pierre, T., Paquette, J.L., Vanardois, J., 2020. Contribution of magmatism, partial melting buffering and localized crustal thinning on the late Variscan thermal structure of the Agly Massif French Pyrenees. J. Metamorph. Geol. 38, 799–829.

Stefánsson, A., Seward, T.M., 2004. Gold (I) complexing in aqueous sulphide solutions to 500°C at 500 bar. Geochim. Cosmochim. Acta 68, 4121–4143.

Snee, L.W., 2002. Argon thermochronology of mineral deposits – a review of analytical methods, formulations, and selected applications. U.S Geol. Surv, Bull, p. 2194.

Sośnicka, M., Lüders, V., Duschl, F., Kraemer, D., Laurent, O., Niedermann, S., Banks, D. A., Wilke, F., Ueberwasser, C.W., Wiedenbeck, M., 2023. Metal budget and origin of aqueous brines depositing deep-seated Zn-Pb mineralization linked to hydrocarbon reservoirs, north German Basin. Miner. Depos. 58, 1143–1170.

Stipp, M., Stünitz, H., Heilbronner, R., Schmid, S.M., 2002. The eastern Tonale fault zone: a 'natural laboratory' for crystal plastic deformation of quartz over a temperature range from 250-700°C. J. Struct. Geol. 24, 1861–1884.

Ternois, S., Odlum, M., Ford, M., Pik, R., Stockli, D.F., Tibari, B., Vacherat, A., Bernard, V., 2019. Thermochronological evidence of early orogenesis, eastern Pyrenees, France. Tectonics 38, 1308–1336.

Tischendorf, G., Gottesmann, B., Förster, H.-J., Trumbull, R.B., 1997. On Li-bearing micas: estimating Li from electron microprobe analyses and an improved diagram for graphical representation. Mineral. Mag. 408, 809–834.

Tournaire, G.B., Olivier, P., Paquette, J.L., Bosse, V., Guillaume, D., 2018. Evolution of the middle crust of the Pyrenees during the Paleozoic: New data on the plutonic rocks from the North Pyrenean Agly Massif. J. Int. Earth Sci. 108, 245–265.

Turner, G., Wang, S.S., 1992. Excess argon, crustal fluids and apparent isochrons from crushing K-feldspar. Earth Planet. Sci. Lett. 110, 193–211.

Vanardois, J., Trap, P., Roger, F., Goncalves, P., Marquer, D., Paquette, J.L., Siron, G., Baudin, T., 2022. Flow of the partially molten crust of the Variscan foreland revealed by U–TH–Pb dating of metamorphism, magmatism and deformation (Agly Massif, Eastern Pyrenees). J. Int. Earth Sci. 111, 2101–2128.

Van den Eeckhout, B., Zwart, H.J., 1988. Hercynian crustal scale extensional shear zone in the Pyrenees. Geology 16, 135–138.

Vauchez, A., Clerc, C., Bestani, L., Lagabrielle, Y., Chauvet, A., Lahfid, A., Mainprice, D., 2013. Preorogenic exhumation of the North Pyrenean Agly Massif (Eastern Pyrenees-France). Tectonics 32, 95–106.

Verschure, R.H., Andriessen, P.A.M., Boelrijk, N.A.I.M., Hebeda, E.H., Maijer, C., Priem, H.N.A., Verdurmen, E.A.T., 1980. On the thermal stability of Rb-Sr and K-Ar biotite systems: evidence from coexisting Sveconorwegian (ca 870 Ma) and Caledonian (ca 400 Ma) biotites in SW Norway. Contrib. Mineral. Petrol. 74, 245–252.

Vielzeuf, D., Kornprobst, J., 1984. Crustal splitting and the emplacement of the Pyrenean lherzolites and granulites. Earth Planet. Sci. Lett. 67, 87–96.

Villa, I.M., Bucher, S., Bousquet, R., Kleinhanns, I.C., Schmid, S.M., 2014. Dating polygenetic metamorphic assemblages along a Transect across the Western Alps. J. Petrol. 55, 803–830.

Vissers, R.L.M., 1992. Variscan extension in the Pyrenees. Tectonics 11, 1369–1384.

Whitchurch, A.L., Carter, A., Sinclair, H.D., Duller, R.A., Whittaker, A.C., Allen, P.A., 2011. Sediment routing system evolution within a diachronously uplifting orogen: Insights from detrital zircon thermochronological analyses from the South-Central Pyrenees. J. Am. Soc. 311, 442–482.

Wickham, S.M., Taylor Jr., H.P., 1985. Stable isotopic evidence for large-scale seawater infiltration in a regional metamorphic terrane; the Trois Seigneurs Massif, Pyrenees, France. Contrib. Mineral. Petrol. 91, 122–137.

Wijbrans, J.R., Pringle, M.S., Koppers, A.A.P., Scheveers, R., 1995. Argon geochronology of small samples using the Vulkaan argon laserprobe. Proc. k. Ned. Akad. Wetensch 98, 185–218.

Wiewióra, A., Weiss, Z., 1990. Crystallochemical classifications of phyllosilicates based on the unified system of projection of chemical composition: II. The Chlorite Group. Clay Miner. 25, 83–92.

Xiao, M., Qiu, H., Jiang, Y.D., Cai, Y., Bai, X., Zhang, W., Liu, M., Qin, C.J., 2019. Gas release systematics of mineral hosted fluid inclusions during stepwise crushing: implications for [40]Ar/[39]Ar geochronology of hydrothermal fluids. Geochim. Cosmochim. Acta 251, 36–55.

Xiao, M., Jiang, Y.D., Qiu, H., Cai, Y., Zhang, W.F., 2022a. An improved gas extraction model during stepwise crushing: New perspective on fluid geochronology and geochemistry. Ore Geol. Rev. 140, 104588.

Xiao, M., Jiang, Y., Zhao, G., Qiu, H., Cai, Y., Bai, X., Yuan, C., Zhang, W., Kong, L., Wang, S., 2022b. Fluid inclusions [40]Ar/[39]Ar geochronology of andalusite from syn-tectonic quartz veins: New perspective on dating deformation and metamorphism in low-pressure metamorphic belts. Geochim. Cosmochim. Acta 323, 141–163.

Yardley, B.W.D., 1983. Quartz veins and devolatilization during metamorphism. J. Geol. Soc. London 140, 657–663.

Yelland, A.J., 1990. Fission track thermotectonics in the Pyrenean orogen. Nucl. Tracks Radiat. Meas. 17, 293–299.

Yu, X., Wang, C., Huang, H., Wang, J., Yan, K., 2023. Lithium and brine geochemistry in the Qianjiang formation of the Jianghan basin, Central China. Sci. Rep. 13, 4445.

Zwart, H.J., 1979. The geology of the central Pyrenees. Leidse Geol. Meded. 50, 1–174.